ARTICLES
https://doi.org/10.1038/s41594-022-00792-w

nature structural & molecular biology

Architecture of the human erythrocyte ankyrin-1 complex

Francesca Vallese[1,2,3], Kookjoo Kim[1,2,3], Laura Y. Yen[2], Jake D. Johnston[2,4], Alex J. Noble[4], Tito Calì[5,6,7] and Oliver Biggs Clarke[1,2,3] ✉

The stability and shape of the erythrocyte membrane is provided by the ankyrin-1 complex, but how it tethers the spectrin–actin cytoskeleton to the lipid bilayer and the nature of its association with the band 3 anion exchanger and the Rhesus glycoproteins remains unknown. Here we present structures of ankyrin-1 complexes purified from human erythrocytes. We reveal the architecture of a core complex of ankyrin-1, the Rhesus proteins RhAG and RhCE, the band 3 anion exchanger, protein 4.2, glycophorin A and glycophorin B. The distinct T-shaped conformation of membrane-bound ankyrin-1 facilitates recognition of RhCE and, unexpectedly, the water channel aquaporin-1. Together, our results uncover the molecular details of ankyrin-1 association with the erythrocyte membrane, and illustrate the mechanism of ankyrin-mediated membrane protein clustering.

An ordered lattice of spectrin and actin gives mechanical stability and shape to otherwise fragile cellular membranes. The periodic spectrin–actin cytoskeleton was first identified in erythrocytes[1], but has since been found in other cell types, including neurons[2]. The spectrin–actin network is tethered to the membrane by giant, spring-like proteins known as ankyrins, which also serve the purpose of clustering diverse membrane proteins at specific subcellular locations.

Three ankyrin proteins are present in vertebrates: ankyrin-1 (ankyrin-R), ankyrin-2 (ankyrin-B) and ankyrin-3 (ankyrin-G). Ankyrins share a common domain arrangement, consisting of a highly conserved N-terminal membrane binding domain with 24 ankyrin repeats (AR1-24), followed by a spectrin binding module (ZU5-ZU5-UPA; ZZU) and a death domain of unclear function. The characteristic 24-repeat membrane binding domain of ankyrins has a groove on the inner concave surface that mediates recruitment of short peptides from target proteins, as well as mediating autoinhibition by regions of the MBD-ZZU linker and the C-terminal tail. Ankyrin-1 was first identified in erythrocytes[3], where it mediates the attachment of the band 3 anion transport protein (AE1; SLC4A1) to spectrin[4]. It is also found in other tissues, including skeletal muscle and brain, where it has recently been shown to mediate clustering of Kv3.1b K^+ channels in specific neuronal subtypes[5]. Ankyrin-2 and 3 play pivotal roles as dynamic adaptor platforms in cardiomyocytes and striated muscle cells[6], and in neurons of the central[7] and peripheral[8] nervous systems, respectively.

In erythrocytes, ankyrin-1 attaches the cytoskeleton to the membrane via direct interaction with spectrin[9], and additionally mediates clustering of integral membrane proteins, helping maintain the structure of the membrane and coordinating the spatial organization of transporters and channels involved in the regulation of cellular volume and cytosolic composition. Mutations in components of the erythrocyte ankyrin-1 complex are linked to an inherited anemia known as hereditary spherocytosis, in which the characteristic biconcave disc shape of healthy erythrocytes is lost, resulting in small, fragile, spherical cells known as spherocytes[10]. Ankyrin and spectrin mutations are also associated with several other genetic diseases, including neurological and cardiac abnormalities[11]. The erythrocyte ankyrin-1 complex is known to contain the band 3 chloride/bicarbonate exchanger, the adaptor molecule protein 4.2, the single transmembrane proteins glycophorin A (GPA) and glycophorin B (GPB), and the Rhesus proteins RhAG and RhCE[12]. Other proteins that are believed to associate with the ankyrin-1 complex include GLUT1 (ref. [13]), LW and CD-47 (ref. [14]). However, the stoichiometry and architecture of the complex remains unknown, making it close to impossible to reconstitute recombinantly.

Here, we purified the ankyrin-1 complex from human erythrocytes, and captured a series of high-resolution structures by single-particle cryogenic-electron microscopy (cryo-EM), complemented by a subtomogram average of the complex in the context of native erythrocyte membrane fragments. These revealed its architecture and composition, shedding light on the mechanism of membrane protein recruitment by ankyrin and protein 4.2, and identifying aquaporin-1 as an unanticipated component of the ankyrin-1 complex.

Results

Structure determination of the ankyrin-1 complex. The ankyrin-1 complex was purified from digitonin-solubilized human erythrocyte ghost membranes by density gradient centrifugation, followed by size-exclusion chromatography (Fig. 1a, Supplementary Fig. 1a,b and Supplementary Video 1). The final sample contained a major 1.2-MDa species as assessed by mass photometry[15] (Supplementary Fig. 1c). The presence of main components of the erythrocyte ankyrin-1 complex, including ankyrin-1, band 3, protein 4.2, GPA and RhAG was assessed by SDS–PAGE and confirmed by mass spectrometry analysis (Supplementary Table 1).

Cryo-EM analysis (Table 1) of the purified sample revealed both a mixture of ankyrin-1 containing complexes, as well as smaller

[1]Department of Anesthesiology, Columbia University Irving Medical Center, New York, NY, USA. [2]Department of Physiology and Cellular Biophysics, Columbia University, New York, NY, USA. [3]Irving Institute for Clinical and Translational Research, Columbia University, New York, NY, USA. [4]Simons Electron Microscopy Center, New York Structural Biology Center, New York, NY, USA. [5]Department of Biomedical Sciences, University of Padua, Padua, Italy. [6]Padua Neuroscience Center (PNC), University of Padua, Padua, Italy. [7]Study Center for Neurodegeneration (CESNE), University of Padua, Padua, Italy. ✉e-mail: olibclarke@gmail.com

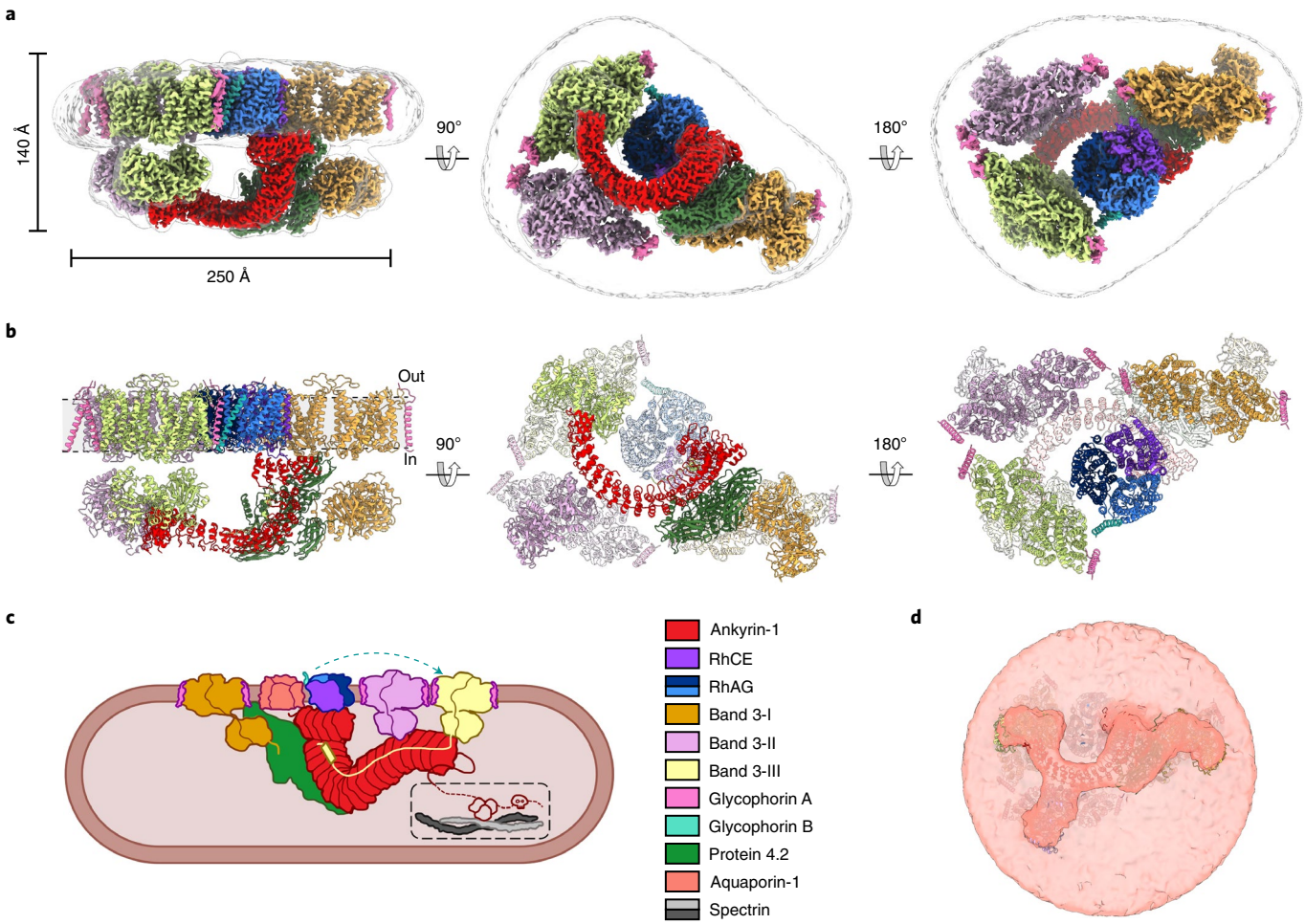

Fig. 1 | Architecture of the human erythrocyte ankyrin-1 complex. a, The overall cryo-EM density map of the ankyrin-1 complex (Class 1a, transparent white surface) shown in three different views, with local reconstructions of different regions superposed. Band 3-I, II, III are colored orange, lilac and yellow, respectively; ankyrin is colored red, protein 4.2 green, RhCE purple and RhAG blue and light blue, GPA is colored in magenta and GPB in aquamarine. **b**, Model of the ankyrin-1 complex in the plane of the membrane (left panel), viewed from the cytoplasm (central panel) and from the outside the plasma membrane (right panel). Reference colors are the same used in **a**. **c**, Schematic of the proposed ankyrin-1 complex in the RBC. Inside the dashed line the connection between ankyrin and spectrin is depicted. **d**, Subtomogram average of the ankyrin-1 complex from native vesicles with rigid body fit atomic model.

complexes of free band 3 with GPA (Extended Data Fig. 1a,b and Supplementary Fig. 1d).

After repicking using a Topaz model trained on the smaller complexes[16], ab initio reconstruction and refinement of the band 3–GPA class gave a C1 reconstruction at 2.8 Å. Both protomers were in the outward open state, and the transmembrane domains exhibit apparent C2 symmetry. Refinement gave a 2.3 Å reconstruction with C2 symmetry applied, allowing us to build a complete atomic model of the band 3–GPA complex (Extended Data Fig. 1c).

Refinement of all 710,000 ankyrin-1-containing particles against an ab initio reference yielded a 2.4 Å consensus reconstruction (Extended Data Fig. 2). Well-ordered density is observed for the Rh heterotrimer, ankyrin-1, protein 4.2 and the cytoplasmic domains of a single band 3 dimer (denoted subsequently as Band 3-I). Masked refinement and in some cases focused three-dimensional- (3D-) variability analysis was used to improve the density quality for each component (Extended Data Fig. 3).

Subclassification of the ankyrin complexes revealed six distinct classes with variable composition (Extended Data Fig. 4a). The core architecture is conserved in all six classes, but with elaborations. Class 1 had a larger micelle than observed in the consensus refinement, accommodating two additional band 3 dimers (denoted Band 3-II and Band 3-III) that interact directly with ankyrin. Two-dimensional (2D) classes of Class 1 resemble complexes identified in native membrane vesicles using cryo-electron tomography (cryo-ET) (Fig. 1d, Extended Data Fig. 5, Supplementary Fig. 2 and Supplementary Videos 2 and 3). Classes 2 and 5 had an additional component present that proved to be an aquaporin-1 (AQP1) tetramer. Class 4 has an overall architecture similar to Class 1, but with a different orientation of the Band 3-I transmembrane region and the presence of an unknown membrane protein.

While the cytoplasmic domains of Band 3-I were well ordered in the consensus refinement, the transmembrane (TM) domains were very poorly resolved, which we rectified using the following classification scheme. After local refinement gave a poor quality 3.8 Å map, 3D-variability analysis was carried out in cryoSPARC using a mask around the Band 3-I TM. Clustering with a single mode corresponding to an order–disorder transition of the transmembrane region allowed identification of a 226,000 particle subset for which local refinement gave a 2.8 Å map with excellent density quality, and a well-resolved interface with protein 4.2 (Extended Data Fig. 6). A similar approach was applied to improve the density of Band 3-II and Band 3-III starting from Class 1, resulting in 3.3 and 3.0 Å local refinements, respectively.

Table 1 | Cryo-EM data collection, refinement and validation statistics

	Ankyrin-1 complex consensus refinement						
	Band3-GPA (PDB 7UZ3) (EMD-26874)	**Composite (PDB 7V0K) (EMD-26943)**	**Rh-AR1-5 (PDB 7UZQ) (EMD-26916)**	**Protein 4.2 (PDB 7UZS) (EMD-26917)**	**Ankyrin N-term (PDB 7UZU) (EMD-26918)**	**Band3-I cytosolic domains (PDB 7UZV) (EMD-26919)**	**Band3-I TM domains (PDB 7V07) (EMD-26940)**
Data collection and processing							
Magnification	105,000x	105,000x	105,000x	105,000x	105,000x	105,000x	105,000x
Voltage (kV)	300	300	300	300	300	300	300
Electron exposure ($e^-/Å^2$)	58	58	58	58	58	58	58
Defocus range (μm)	−0.5 to −1.5	−0.5 to −1.5	−0.5 to −1.5	−0.5 to −1.5	−0.5 to −1.5	−0.5 to −1.5	−0.5 to −1.5
Pixel size (Å)	0.83	0.83	0.83	0.83	0.83	0.83	0.83
Symmetry imposed	C1	C1	C1	C1	C1	C1	C1
Initial micrographs	14,926	14,926	14,926	14,926	14,926	14,926	14,926
Final micrographs	14,464	14,464	14,464	14,464	14,464	14,464	14,464
Initial particle images	1,781,329	1,781,329	1,781,329	1,781,329	1,781,329	1,781,329	1,781,329
Final particle images	166,626	710,437	710,437	710,437	710,437	710,437	226,351
Map resolution (Å)	2.33	2.39	2.17	2.20	2.34	2.47	2.82
FSC threshold	0.143	0.143	0.143	0.143	0.143	0.143	0.143
Map sharpening *B* factor ($Å^2$)	−47.7	−42.5	−52.5	−56.5	−65.5	−70.1	−80.1
Model composition							
Non-hydrogen atoms	9,315	32,037	10,403	5,367	3,744	4,682	9,162
Protein residues	1,114	3,997	1,315	658	483	584	1,114
Ligand molecules	20	14	4	0	0	0	20
R.m.s. deviations							
Bond lengths (Å)	0.0054	0.0039	0.0062	0.0043	0.0029	0.0027	0.0059
Bond angles (°)	0.76	0.68	0.91	0.72	0.57	0.58	0.90
Validation							
Clashscore	2.87	7.29	4.49	2.70	3.14	3.69	8.34
Poor rotamers (%)	0.84	2.26	2.27	1.79	0.52	2.84	3.89
Ramachandran plot							
Favored (%)	97.82	98.07	97.99	98.92	96.87	98.26	97.91
Allowed (%)	2.18	1.80	1.78	1.08	3.13	1.39	1.81
Disallowed (%)	0	0.13	0.23	0	0	0.35	0.27

Continued

Table 1 | Cryo-EM data collection, refinement and validation statistics (continued)

	Class 1											
	Composite (PDB 8CS9) (EMD-26960)	Rh-AR1-5 (PDB 7V0S) (EMD-26949)	Protein 4.2 (PDB 7V0Q) (EMD-26948)	Ankyrin N-term (PDB 7V0M) (EMD-26944)	Ankyrin C-term (PDB 7V0X) (EMD-26952)	Band3-I cytosolic domain (PDB 7V0T) (EMD-26950)	Band3-II cytosolic domain (PDB 7V0U) (EMD-26951)	Band3-III cytosolic domain (PDB 7V0Y) (EMD-26953)	Band3-I TM (PDB 8CRQ) (EMD-26955)	Band3-II TM (PDB 7V19) (EMD-26954)	Band3-III TM (PDB 8CRR) (EMD-26956)	Rh-GPB (PDB 8CRT) (EMD-26958)
Data collection and processing												
Magnification	105,000x	105,000x	105,000x	105,000x	105,000x	105,000x	105,000x	105,000x	105,000x	105,000x	105,000x	105,000x
Voltage (kV)	300	300	300	300	300	300	300	300	300	300	300	300
Electron exposure ($e^-/Å^2$)	58	58	58	58	58	58	58	58	58	58	58	58
Defocus range (μm)	−0.5 to −1.5	−0.5 to −1.5	−0.5 to −1.5	−0.5 to −1.5	−0.5 to −1.5	−0.5 to −1.5	−0.5 to −1.5	−0.5 to −1.5	−0.5 to −1.5	−0.5 to −1.5	−0.5 to −1.5	−0.5 to −1.5
Pixel size (Å)	0.83	0.83	0.83	0.83	0.83	0.83	0.83	0.83	0.83	0.83	0.83	0.83
Symmetry imposed	C1	C1	C1	C1	C1	C1	C1	C1	C1	C1	C1	C1
Initial micrographs	14,926	14,926	14,926	14,926	14,926	14,926	14,926	14,926	14,926	14,926	14,926	14,926
Final micrographs	14,464	14,464	14,464	14,464	14,464	14,464	14,464	14,464	14,464	14,464	14,464	14,464
Initial particle images	710,437	710,437	710,437	710,437	710,437	710,437	710,437	710,437	710,437	710,437	710,437	710,437
Final particle images	126,197	126,197	126,197	126,197	126,197	126,197	126,197	126,197	85,645	44,624	96,966	22,953
Map resolution (Å)	2.75	2.44	2.44	2.65	2.97	2.71	3.0	2.95	3.14	3.33	2.96	3.0
FSC threshold	0.143	0.143	0.143	0.143	0.143	0.143	0.143	0.143	0.143	0.143	0.143	0.143
Map sharpening *B* factor ($Å^2$)	−35.1	−57.5	−58.7	−65.9	−84.7	−79.2	−101.2	−104.3	−83.1	−79.7	−77.4	−39.9
Model composition												
Non−hydrogen atoms	60,944	10,303	5,301	3,724	2,818	4,658	4,453	4,454	8,936	8,936	8,936	17,925
Protein residues	7,677	1,315	658	483	375	584	558	558	1,114	1,114	1,114	2,305
Ligand molecules	27	3	0	0	0	0	0	0	8	8	8	6
R.m.s. deviations												
Bond lengths (Å)	0.0063	0.0042	0.0036	0.0034	0.0023	0.0037	0.0050	0.0031	0.0035	0.0022	0.0041	0.0032
Bond angles (°)	1.16	0.72	0.61	0.56	0.63	0.63	0.75	0.63	0.56	0.49	0.57	0.58
Validation												
Clashscore	7.77	5.04	3.48	3.55	6.52	6.19	7.40	5.27	4.15	4.97	4.26	5.01
Poor rotamers (%)	3	2.55	2.15	1.29	5.05	3.45	2.50	1.46	1.37	1.16	0.95	2.36
Ramachandran plot												
Favored (%)	97.36	98.22	98.92	96.66	95.96	98.26	98.54	98.54	98.46	98.37	97.91	98.50
Allowed (%)	2.42	1.70	1.08	3.34	4.04	1.57	1.46	1.46	1.54	1.63	2.09	1.45
Disallowed (%)	0.22	0.08	0	0	0	0.17	0	0	0	0	0	0.04

Continued

Table 1 | Cryo-EM data collection, refinement and validation statistics (continued)

	Class 2									
	Composite (PDB 8CTE) (EMD-26988)	**Rh (PDB 8CSX) (EMD-26974)**	**Protein 4.2 (PDB 8CSW) (EMD-26973)**	**Ankyrin N-term (PDB 8CSV) (EMD-26972)**	**Band3-I cytosolic domain (PDB 8CSY) (EMD-26975)**	**Band3-I TM (PDB 8CT3) (EMD-26979)**	**AQP1 (C1) (PDB 8CT2) (EMD-26978)**	**AQP1 (C4) (PDB 7UZE) (EMD-26886)**	**Class 4 (EMD-26982)**	**SubTomo (PDB 8CSL) (EMD-26965)**
Data collection and processing										
Magnification	105,000x	105,000x	105,000x	105,000x	105,000x	105,000x	105,000x	105,000x	105,000x	41,960x
Voltage (kV)	300	300	300	300	300	300	300	300	300	300
Electron exposure (e^-/Å^2)	58	58	58	58	58	58	58	58	58	112
Defocus range (μm)	−0.5 to −1.5	−0.5 to −1.5	−0.5 to −1.5	−0.5 to −1.5	−0.5 to −1.5	−0.5 to −1.5	−0.5 to −1.5	−0.5 to −1.5	−0.5 to −1.5	−3.5 to −4.5
Pixel size (Å)	0.83	0.83	0.83	0.83	0.83	0.83	0.83	0.83	0.83	2.077
Symmetry imposed	C1	C1	C1	C1	C1	C1	C1	C4	C1	C1
Initial micrographs	14,926	14,926	14,926	14,926	14,926	14,926	14,926	14,926	14,926	100
Final micrographs	14,464	14,464	14,464	14,464	14,464	14,464	14,464	14,464	14,464	100
Initial particle images	710,437	710,437	710,437	710,437	710,437	710,437	710,437	710,437	710,437	60,029
Final particle images	145,645	145,645	145,645	145,645	145,645	71,451	145,645	108,425	51,283	1596
Map resolution (Å)	2.90	2.40	2.47	2.73	2.71	3.32	3.04	2.42	4.1	24.6
FSC threshold	0.143	0.143	0.143	0.143	0.143	0.143	0.143	0.143	0.143	0.143
Map sharpening *B* factor (Å^2)	−40.8	−59.7	−60.7	−75.1	−68.6	−77.1	−85.0	−68.6	−60.1	NA
Model composition										
Non-hydrogen atoms	38,844	9,116	5,332	3,712	4,638	8,964	7,464	7,577	-	30,720
Protein residues	4,984	1,158	657	483	584	1,114	988	988	-	7,677
Ligand molecules	16	4	0	0	0	8	4	4	-	0
R.m.s. deviations										
Bond lengths (Å)	0.0024	0.0056	0.0065	0.0023	0.0030	0.0020	0.0038	0.0032	-	NA
Bond angles (°)	0.52	0.77	0.86	0.47	0.56	0.48	0.61	0.58	-	NA
Validation										
Clashscore	5.53	4.87	4.93	2.73	4.67	4.29	4.61	3.56	-	NA
Poor rotamers (%)	2.00	2.00	2.33	1.03	4.06	0.63	2.03	0.68	-	NA
Ramachandran plot										
Favored (%)	98.27	98.24	98.76	97.08	98.43	99.09	97	96.59	-	NA
Allowed (%)	1.61	1.67	1.24	2.71	1.57	0.91	2.58	3.00	-	NA
Disallowed (%)	0.12	0.09	0	0.21	0	0	0.41	0.41	-	NA

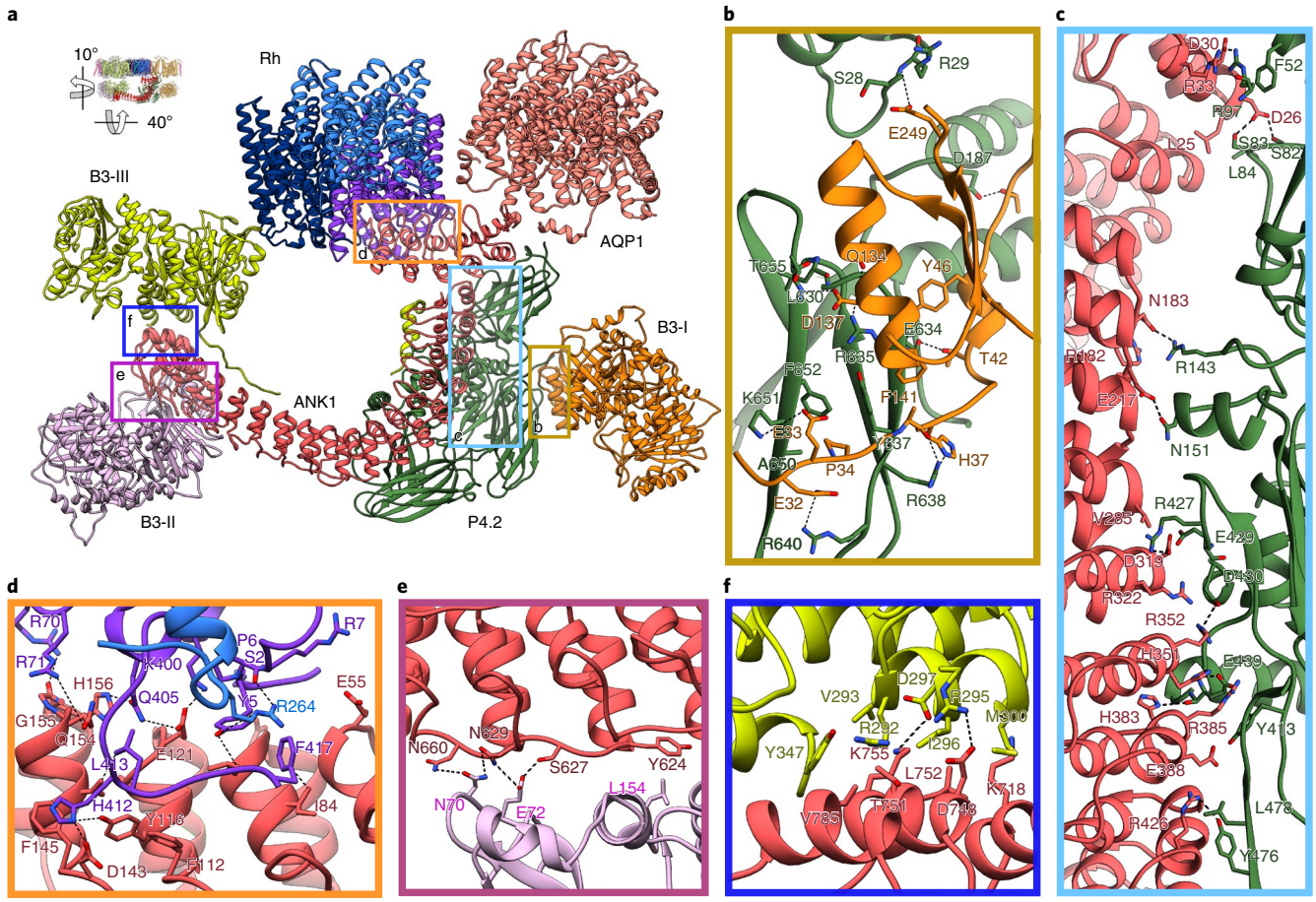

Fig. 2 | Interactions between ankyrin-1 and the proteins in the ankyrin-1 complex. a, Overview of ankyrin-1 interactions with binding partners in the ankyrin-1 complex. The proteins are depicted in cartoon representation. Transmembrane domains of band 3, GPA and GPB are omitted for clarity. Ankyrin (red) interacts with RhCE (purple) and AQP1 (salmon), and both interact with the peptide binding groove of AR1-5; protein 4.2 (green) interacts with the exterior surface of AR1 and AR6-13; Band 3-II (B3-II) (lilac) and Band 3-III (B3-III) (yellow) interact predominantly with the exterior surface of AR17-24, the N terminus domain of Band 3-III also interacts with the peptide binding groove of AR6-10. Insets refer to regions highlighted in **b**–**f**. On the top left of **a**, a small thumbnail is included to show how the figure is positioned compare to Fig. 1a. **b**–**f**, Close-up views of the interactions between protein 4.2 and Band 3-I (orange) (**b**); ankyrin and protein 4.2 (**c**); ankyrin and RhCE (**d**); ankyrin and Band 3-II (**e**) and ankyrin and Band 3-III (**f**). The key residues that mediate the interactions in the interfaces are shown as sticks. Key interactions are indicated with black dotted lines.

By applying this clustering approach to Class 2, a particle subset was identified with improved AQP1 density, resulting in a 3.0 Å C1 map that facilitated unambiguous fitting of the AQP1 crystal structure, and identification of the regions of AQP1 that interact with ankyrin-1 and protein 4.2. Application of local C4 symmetry yielded a 2.4 Å map (Supplementary Video 4).

We have used the reconstructions described above to build atomic models for class 1a (Fig. 1b), which we believe represents an intact complex, and class 2, in which the interaction with AQP1 is best defined, as well as for the consensus refinement of all classes, which had the best resolved density at the core of the complex. AQP1 is present in classes 2 and 5. The remaining classes may represent genuine diversity in the composition of complexes present in the membrane, or partial dissociation of a single native complex (Extended Data Fig. 4a). The association of AQP1 in classes 2 and 5 appears compatible with the arrangement of band 3 dimers in Class 1, despite a substantial rigid body rearrangement of the transmembrane domains of Band 3-I in the presence of AQP1 (Extended Data Fig. 4b). We therefore assess that in vivo, the three band 3 dimers identified here, as well as AQP1, are likely to be part of the same complex. This conclusion is supported by analysis of tomograms obtained from vesicles generated by extrusion of native erythrocyte membranes. The appearance of particles in the tomograms is very similar to the 2D classes obtained by single-particle analysis (Supplementary Video 2), and subtomogram averaging of particles extracted from the tomograms identifies a class with near identical architecture to Class 1/1a (Fig. 1d, Supplementary Fig. 2a,b and Supplementary Video 3). The absence of CD-47 and LW from the complex may indicate that they are loosely associated, and lost during digitonin extraction, or that they are associated with a distinct complex that we have not isolated.

Architecture of the human erythrocyte ankyrin-1 complex. The architecture of Class 1a is presented in Fig. 1 and Supplementary Video 1. The membrane-embedded core of the complex is formed by the $(RhAG)_2$(RhCE) heterotrimer. Ankyrin binds to the N and C termini of RhCE, via the first five ankyrin repeats (AR1-5), which are oriented parallel to the membrane. The subsequent ankyrin repeats (AR6-24) emerge perpendicularly downward from a T interface with AR1-5, and gradually recurve to run almost parallel to the membrane.

Protein 4.2 is oriented vertically, such that the myristoylated N terminus contacts the membrane, with one flat surface bound to AR1 and AR6-13 of ankyrin, while the distal face recruits band 3.

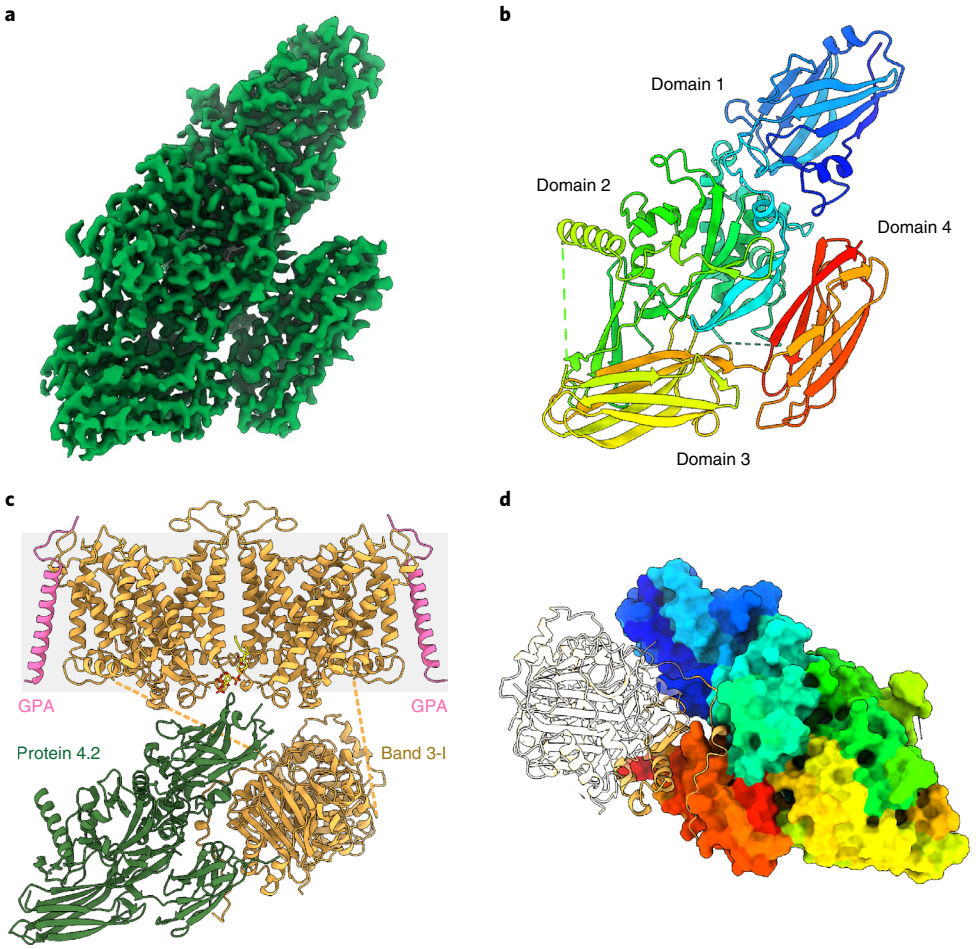

Fig. 3 | Protein 4.2 is an adaptor that mediates binding of Band 3-I. a, The 2.4 Å cryo-EM density map of protein 4.2 from local refinement of the consensus reconstruction. **b**, Structure of protein 4.2 colored by domain from the N (blue) to the C (red) terminus. The four domains are labeled. The proteins are depicted as cartoon representations. **c**, Model of protein 4.2 (green) and band 3-I (orange), PIP_2 is colored in yellow. The proteins are shown as cartoon representations, and the membrane is represented in gray. **d**, The outer face of protein 4.2 forms the primary binding site for Band 3-I. Protein 4.2 is displayed as a molecular surface colored by domain from the N (blue) to the C (red) terminus, band 3-I cytosolic domain is displayed as ribbon and the parts of Band 3-I that are not interacting with protein 4.2 are shown in transparency.

Three band 3–GPA dimers (Band 3-I, Band 3-II and Band 3-III) form part of the complex. Band 3-I binds to the distal face of protein 4.2 via the band 3 cytoplasmic domain and N-terminal peptide. Band 3-II and Band 3-III, by contrast, both interact directly with ankyrin. Band 3-II interacts with the outer face of AR17-19 via the cytoplasmic domain, while the cytoplasmic domain of Band 3-III binds to the outer face of AR21-24 and the Band 3-III N-terminal peptide runs back along the inner groove of ankyrin.

Membrane association and target recruitment by ankyrin-1. We observe simultaneous engagement of the ankyrin-1 membrane binding domain with multiple targets (Fig. 2a) that fall into three distinct categories: membrane embedded (RhCE and AQP1), extramembrane (cytosolic domains of band 3) and peripheral adapters (protein 4.2). The integral membrane targets, RhCE and AQP1, both interact with the peptide binding groove of AR1-5, the adaptor (protein 4.2) interacts with the exterior surface of AR1-13 and the two extramembrane targets (Band 3-II and Band 3-III) interact predominantly with the exterior surface of AR17-24, supplemented in the case of Band 3-III by interactions of the N terminus with the peptide binding groove of AR6-10.

The Rh heterotrimer forms the primary membrane attachment site for ankyrin-1, mediated via an interaction between the N and C termini of RhCE and the first five repeats of ankyrin-1 (Fig. 2d). The structure of ankyrin-1 in the complex (Extended Data Fig. 7a) adopts a T-shaped arrangement in which AR1-5 are orthogonal to AR6-24, with the peptide binding groove of AR1-5 oriented toward the membrane. This is distinct from the extended conformation observed for ankyrin-2 bound to autoinhibitory motifs[17] (Extended Data Fig. 7b). Comparison of the structures of AR1-9 of ankyrin-2 bound to a peptide from the NaV1.2 channel[18], an ankyrin membrane target, with structures bound to the autoinhibitory peptide, shows substantial flexibility at the AR5-6 interface (Extended Data Fig. 7b,c), albeit not to the extent seen here in ankyrin-1. A sequence alignment of the 24 repeats of ankyrin-1 (Extended Data Fig. 7e) shows that, while AR5 and AR6 are highly conserved when compared to the equivalent regions of ankyrin-2 and ankyrin-3 (Extended Data Fig. 7f), they are the most divergent of the ankyrin repeats when compared with the other repeats in the ankyrin-1 MBD. The rearrangement of the AR1-5 module orients the canonical protein binding groove to directly face the membrane, to bind the membrane-embedded targets RhCE (in all classes) and AQP1 (classes 2 and 5) (Extended Data Fig. 4a).

Protein 4.2 forms multiple sites of attachment to ankyrin-1, all of which are outside the canonical peptide binding groove (Fig. 2c). Protein 4.2 acts as an adaptor molecule and a stabilizer for ankyrin,

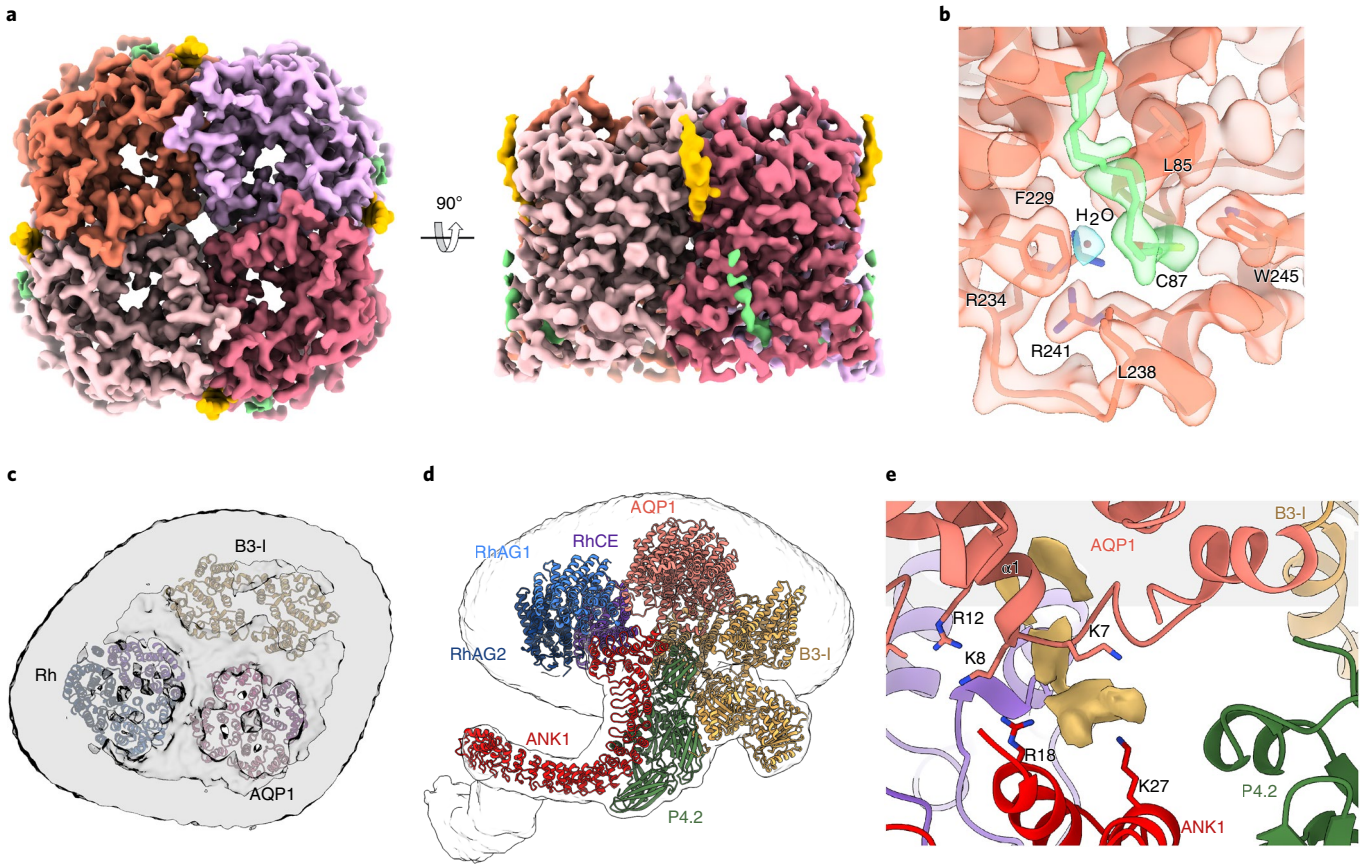

Fig. 4 | Aquaporin is a component of the ankyrin-1 complex. a, The 2.8 Å cryo-EM density map of the aquaporin in Class 2. Densities corresponding to the four subunits are colored in light orange, deep pink, medium purple and hot pink. **b**, Close up of AQP1 palmitoylation of Cys 87. **c**, Aquaporin-1 is present in classes 2 and 5 (Extended Data Fig. 5). The cryo-EM density map of Class 2 shows inside the membrane the density and atomic models corresponding to aquaporin (salmon), Rh (purple, blue and light blue) and Band 3-I (orange). **d**, The model of Class 2 shows that AQP1 (salmon color) is located at the mutual interface of protein 4.2 (green), ankyrin (red), RhCE (purple) and Band 3-I (orange). **e**, Close up of the interaction region between AQP1, protein 4.2 and ankyrin. The membrane is represented in gray. The key residues that mediate the interactions in the interfaces are shown as sticks. Unmodeled density of putative lipid headgroups is shown as an orange surface.

with the outer face of protein 4.2 forming the attachment site for Band 3-I (Fig. 2b). Interaction of domain 1 of protein 4.2 with the exposed 'edge' of AR1 appears to further stabilize the T-shaped conformation of the ankyrin-1 membrane binding domain (Fig. 2c).

In Class 1, Band 3-II and Band 3-III directly bind to ankyrin, interacting with repeats 17–19 and 21–24, respectively (Fig. 2e,f). The N terminus of Band 3-III runs back along the inner ankyrin groove, with residues 2–24 forming an ordered interaction with AR6-10 and the AR5-6 linker (Extended Data Fig. 8a–c and Supplementary Video 5). This peptide is reversed when compared to the binding mode of ankyrin autoinhibitory motifs (Extended Data Fig. 8d–f), but in the same direction as the NaV 1.2 N-terminal peptide bound to ankyrin-2 (ref. [18]) (Extended Data Fig. 7d). The orientation of the Band 3-I cytoplasmic domains is inverted with respect to the membrane when compared with Band 3-II and Band 3-III, which are both directly bound by ankyrin (Extended Data Fig. 9a). Interacting surfaces of band 3 cytoplasmic domains are distinct and nonoverlapping (Extended Data Fig. 9b).

Structure of protein 4.2 and interactions with band 3. The 2.2 Å structure of protein 4.2 is solved here in the context of the ankyrin-1 complex (Fig. 3a,b). As previously suggested[19,20], the fold of protein 4.2, is very similar to that of the closed conformation of tissue transglutaminase (TG2). The central papain-like domain (domain 2) is surrounded by three Ig-like domains (domains 1, 3 and 4). The N-terminal glycine of protein 4.2 is known to be myristoylated[21], and here we see that the N terminus directly contacts the membrane. The inner face of protein 4.2 interacts with ankyrin-1, while the outer face forms the primary binding site for Band 3-I (Fig. 3c,d). The Band 3-I binding mode shares some broad similarities with the binding mode of Band 3-II to ankyrin (Extended Data Fig. 9b), insofar as it involves recognition of a 3D epitope via an extensive interface and is augmented by interaction of the free N terminus of band 3 with a peptide recognition groove. The interaction with Band 3-I is mediated by interactions with D4 and D1 of protein 4.2 (Fig. 2b), and the N terminus of Band 3-I is nestled in a groove formed by D1, D2 and D4. In Class 2, D1 of protein 4.2 also appears to be forming interactions with AQP1. D1 is also forming an interface with loops near the transmembrane dimerization interface of Band 3-I, in a region that also forms cytoplasmic-TM contacts in Band 3-II (Extended Data Fig. 9c).

Aquaporin is a component of the ankyrin-1 complex. A final resolution of 2.5 Å after local refinement with C4 symmetry allows unambiguous fitting of the crystal structure of AQP1 to the density map (Fig. 4a). Clear density is seen for waters in the pore (Extended Data Fig. 10a), as well as a lipid-like density directly attached to Cys-87, which we have assigned as a palmitoylation

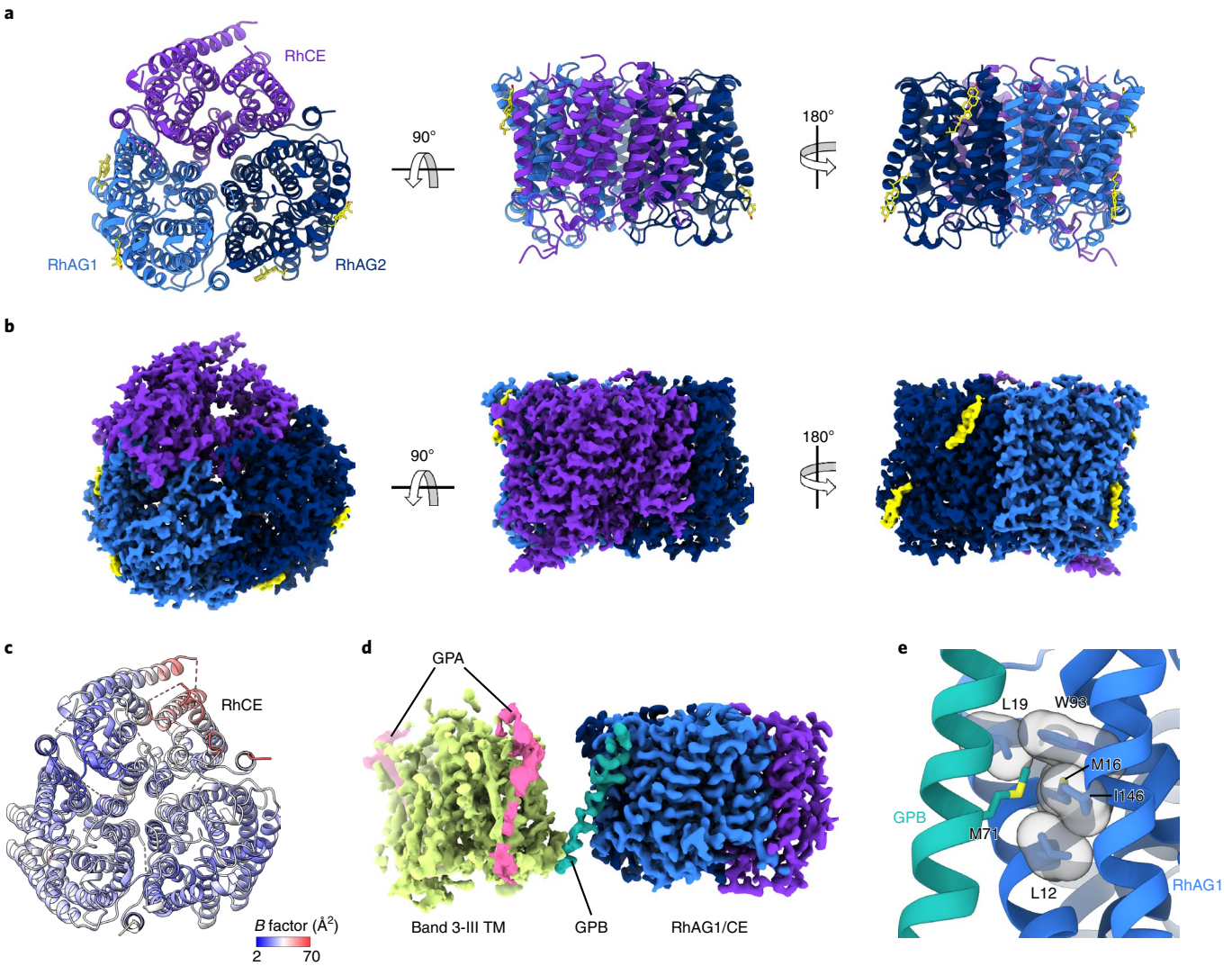

Fig. 5 | $(RhAG)_2(RhCE)$ trimer. a, The structure of the $(RhAG)_2(RhCE)$ trimer as viewed from the cytoplasm (right panel), and as viewed in the plane membrane (central and right panels). RhCE is colored in purple, RhAG1 in light blue and RhAG2 in dark blue. Two molecules of cholesterol (yellow) are bound to each RhAG. **b**, The 2.4 Å cryo-EM density map of the $(RhAG)_2(RhCE)$ complex. Densities corresponding to RhCE, RhAG1 and RhAG2 and cholesterol are colored as in **a**. **c**, Refined atomic *B* factors, averaged per residue. RhCE has higher *B* factors than RhAG, likely indicating more flexibility/mobility. **d**, Cryo-EM density map of the Band 3-III-GPA, $(RhAG)_2(RhCE)$ and GPB that mediates the interaction between the two. **e**, Close up of the interaction region between GPB and RhAG1. The side chain of M71 is located in a hydrophobic pocket in the surface of RhAG1, and the key residues that mediate the interactions are shown as sticks.

site (Fig. 4b). AQP1 is located at the mutual interface of Band 3-I, protein 4.2 and AR1-2 (Fig. 4c,d). The interaction appears to be largely mediated by interactions of the N terminus of AQP1 with AR1-2, and interactions of the C terminus of AQP1 with domain 1 of protein 4.2 (Fig. 4e). In addition, strong, unmodeled density is present in the cleft between AQP1 and RhCE, underneath a patch of positively charged residues contributed by ankyrin, suggesting the possibility of a lipid-mediated interaction with ankyrin-1 and the Rh heterotrimer (Extended Data Fig. 10b). The position of the Band 3-I transmembrane domains is altered substantially in the presence of AQP1 as compared to Class 1 or the consensus refinement, with a translation of roughly 16 Å putting it in close contact with AQP1 and breaking the interaction of Band 3-I with protein 4.2.

Structure and composition of the Rh channel. In the structure of the erythrocyte ankyrin-1 complex presented here, we have resolved the structure of the Rh heterotrimer at 2.2 Å (Fig. 5a,b and Extended Data Fig. 3) revealing that it contains two molecules of RhAG and one of RhCE (Extended Data Fig. 10c,d), with the N and C termini of RhCE interacting with ankyrin-1 (Fig. 2d). RhAG also helps stabilize this interaction, as the RhCE termini pack on top of the adjacent RhAG protomers. Several cholesterol and digitonin molecules are bound to the transmembrane regions of both RhAG and RhCE on both leaflets of the membrane (Fig. 5a,b). The pore of RhAG shows the expected twin-histidine motif in the center of the pore (Extended Data Fig. 10e), with a hydrogen bonded network of water molecules similar to that seen in the structures of AmtB and RhCG. The pore of RhCE is open to both the cytosolic and extracellular sides, with only a short central occlusion (Fig. 5c and Extended Data Fig. 10f), raising the possibility that RhCE may have a role in membrane transport. The density for RhCE is also weaker than for RhAG, despite the fact that RhCE is the subunit that directly engages with ankyrin. This weaker density (and correlated higher atomic *B* factors) may indicate flexibility, possibly consistent with an unresolved conformational change corresponding to pore

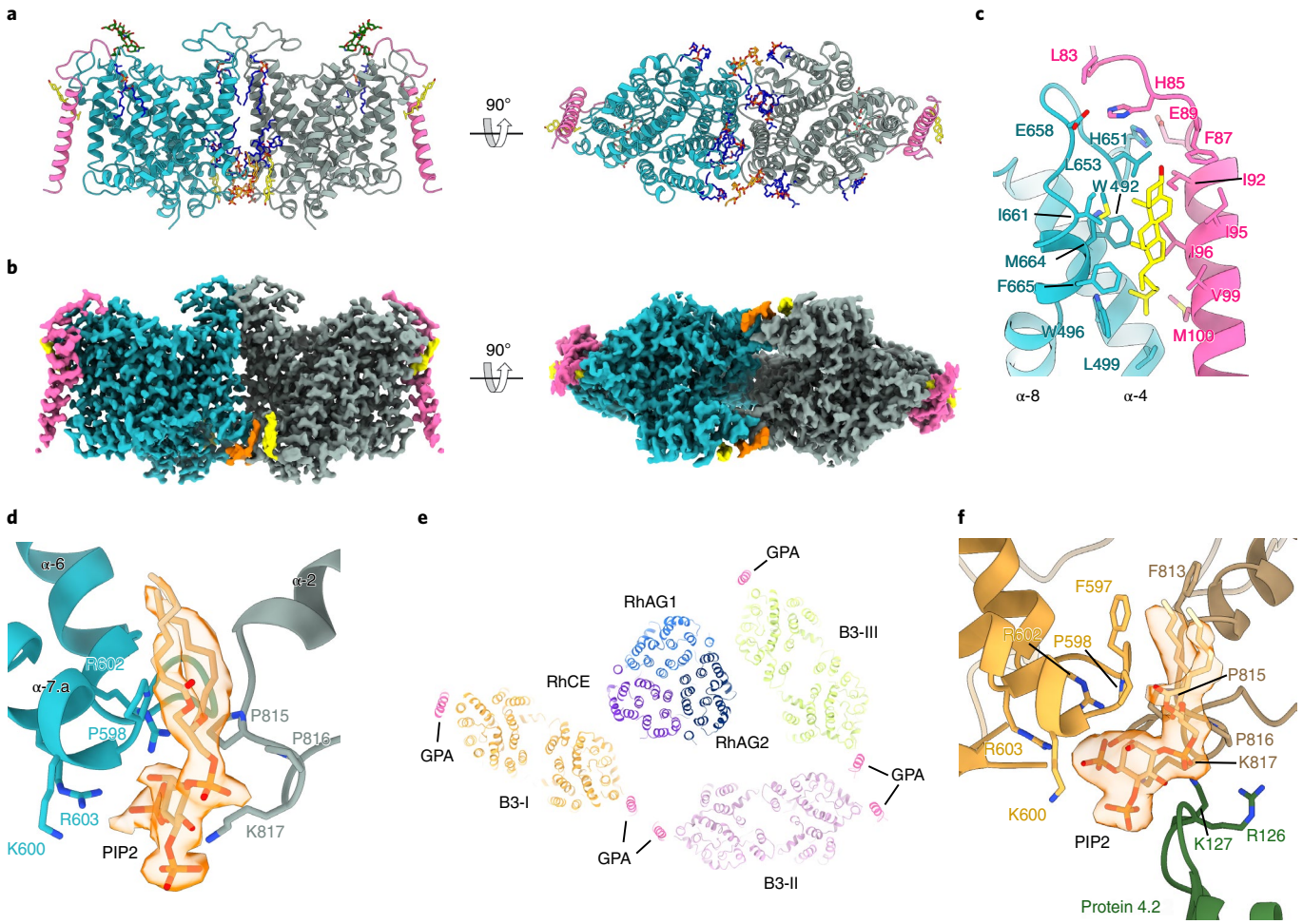

Fig. 6 | Band 3 in complex with GPA. a, The structure of band 3 in complex with GPA as viewed in the plane of the membrane, as viewed from the cytoplasm (central panel) and as viewed from inside the cell. Band 3 protomers are colored aqua green and gray, GPA in magenta and molecules of cholesterol (yellow) PIP_2 (orange) and POPC (blue) are shown. Glycans are colored green. **b**, The 2.3 Å cryo-EM density map of the band 3–GPA complex. Density corresponding to band 3, glycophorin, cholesterol (bound to glycophorin) and PIP_2 are colored as in **a**. The three orientations of the map are the same as **a**. **c**, Close up of the interactions between band 3 (aqua green), glycophorin (magenta) and a cholesterol molecule (yellow). The key residues that mediate the interactions are shown as sticks. **d**, Close up of the band 3 transmembrane dimer interface. PIP_2 (orange) sits in the middle of the site. The key residues that mediate the interactions in the interfaces are shown as sticks. **e**, Cut through the TM of ankyrin-1 complex shows the position of GPA bound to band 3 in the context of the complex. **f**, PIP_2 (orange) sits in the middle of the dimerization site of Band 3-I and close to the interaction site between Band 3-I and protein 4.2. The key residues that mediate the interactions in the interfaces and between Band 3-I TM and protein 4.2 are shown as sticks.

opening (Fig. 5c). Inspection of the map at sites of RhCE/D variation strongly suggests that RhCE is predominantly incorporated (Extended Data Fig. 10h), consistent with previous findings suggesting preferential association of RhCE with the band 3 complex[22].

Local refinement of the Rh trimer in Class 1 revealed an additional transmembrane helix bound to RhAG1 in a groove formed by TM1, TM3 and TM5, with the C terminal end extending toward Band 3-III. Further classification, using a mask around the Rh trimer and Band 3-III, identified a class of 22k particles in which this density was much better defined, allowing assignment as GPB (residues 59–91) (Fig. 5d); however, given the sequence similarity with GPA in the TM region some ambiguity remains in this assignment. The N-terminal half of the helix forms the best-defined interactions with RhAG1, with the side chain of Met71 buried in a hydrophobic pocket formed by Trp93, Ile146, Met16, Leu19 and Leu12 (Fig. 5e). The C-terminal end of the GPB helix (residues 86–91) appears to be forming a weak interaction with the N-terminal juxtamembrane helix of Band 3-III.

Structure of the band 3 dimer complexed with GPA. In the structure of the free band 3 dimer (Fig. 6a,b), a GPA monomer is bound at each end of the band 3 dimer, with the GPA transmembrane helix interacting primarily with TM4 of band 3 and the extracellular N-terminal peptide interacting with the TM7-8 loop (Fig. 6c). A tightly bound cholesterol molecule is located near the extracellular side, wedged between the transmembrane helix of GPA and TM8 of band 3 (Fig. 6c). A prominent lipid headgroup density is located at the intracellular dimer interface of band 3, where it binds to a patch of positively charged residues. Based on the distinctive shape of the density, and previous biochemical data showing enrichment of phosphoinositides in purified band 3 (ref. [23]) we have assigned this density as $PI(4,5)P_2$ (Fig. 6d and Supplementary Video 6). This density is also observed in classes of the intact ankyrin complex, where it is located very close to the interface of Band 3-I with protein 4.2 (Fig. 6e,f).

Discussion

Ankyrins form part of an intricate submembrane lattice that provides mechanical stability, shape and local functional organization to cellular membranes in many cell types including erythrocytes and neurons. In erythrocytes, ankyrin-1 forms the nucleus of a

macrocomplex that acts to tether spectrin to the membrane[3] and organizes several highly abundant membrane proteins involved in gas exchange, pH regulation and control of cellular volume[24] (Supplementary Fig. 3). Mutations in elements of this complex lead to defects in erythrocyte size, shape and stability[10]. However, the architecture and composition of the complex, as well as the mechanism of ankyrin-1 recruitment to the membrane, have so far remained unresolved. Here, we used single-particle cryo-EM to determine structures of an erythrocyte ankyrin-1 complex that includes both the RhAG/CE heterotrimer and band 3. We provide a mechanistic hypothesis for ankyrin recruitment and autoinhibition, showing how ankyrin-1 can recruit three band 3 dimers at distinct sites, clarifying the role of protein 4.2 and identifying aquaporin-1 as an unanticipated component of the ankyrin-1 complex.

Membrane-bound ankyrin-1 adopts a T-shaped conformation. The discontinuous, T-shaped conformation of ankyrin-1 we observe in the membrane-bound state is strongly suggestive of a rearrangement on membrane binding, which we propose is linked to the mechanistic basis of both ankyrin membrane association and autoinhibition. The only previous structure of a full-length ankyrin membrane binding domain is that of ankyrin-2 fused to the autoinhibitory C-terminal tail of ankyrin-1 (ref. [17]), which binds in a continuous groove that traverses the entire length of the molecule. Constructs lacking the autoinhibitory peptide failed to crystallize, likely because they were too conformationally heterogeneous. In contrast, in our structure (Fig. 1a), the ankyrin-1 repeats AR1-5 are oriented parallel to the membrane and orthogonal to the downstream ankyrin repeats. While there is no autoinhibited structure of ankyrin-1 available, the membrane binding domain and the AR5-6 region in particular are highly conserved in all three ankyrin proteins, suggesting that this is unlikely to be an isoform-specific difference. In the ankyrin-2 AR1-24 structure, the autoinhibitory peptide occupies a groove that crosses the AR5-6 boundary, stabilizing them in the 'extended' state. By contrast, in our structure, the N-terminal peptide of Band 3-III occupies this same groove, but ends at the AR5-6 interface, with the very N-terminal 11 residues, including the Syk phosphorylation site Y8, appearing to stabilize it in the T-shaped, 'hammerhead' configuration (Extended Data Fig. 8d and Supplementary Video 5). Deletion of these 11 residues in the band 3 Neapolis mutant causes a severe hemolytic anemia, without compromising insertion into the membrane[25]. Phosphorylation of Y8 also causes alterations in erythrocyte size and shape[26], consistent with a role for this segment in stabilizing the membrane-associated configuration of ankyrin. We hypothesize that the Band 3-III N-terminal peptide displaces the autoinhibitory motif from the inner groove of ankyrin, freeing AR1-5 to adopt the membrane-associated configuration and leaving the AR1-5 groove unoccupied, facilitating recognition of RhCE and AQP1. Band 3-III is also the band 3 dimer that has a GPB-mediated interaction with RhAG1 in Class 1a. It is possible that pre-association of RhAG/CE and Band 3 via GPB could facilitate recruitment of ankyrin-1, with band 3 first displacing the autoinhibition motif, and then AR1-5 binding to RhCE (Supplementary Fig. 4). Binding to protein 4.2 further stabilizes the T-shaped configuration of ankyrin, resulting in the core complex. In this model, the autoinhibited state is not competent to bind to the membrane not only because the inner groove is occupied, but also because AR1-5 are unable to access membrane-embedded targets in the 'extended' state.

Band 3 clustering is mediated by ankyrin-1 and protein 4.2. The ankyrin-1 complex structure reveals four distinct sites of target recruitment (Fig. 2a). We term these sites the juxtamembrane (AR1-5 binding of RhCE and AQP1), the adaptor-mediated (protein 4.2 recruitment of Band 3-I), the central (AR16-18 binding of Band 3-II) and the distal site (Band 3-III binding, including interactions of N-terminal peptide). The observation that band 3 associates directly with ankyrin at the distal and central sites is consistent with studies of AR13-24 binding to the cytoplasmic domain of band 3, which identified a high affinity and a low affinity site[27]. Band 3 has variously been characterized as binding to ankyrin as a bona fide tetramer, or a 'pseudotetramer', in which ankyrin links two band 3 dimers. Our structure is consistent with the latter model. The central site is broadly in agreement with the EPR-based structural model of Kim et al.[28], as well as studies showing the importance of loops 175–185 and 63–73 of the band 3 cytoplasmic domain for interaction with ankyrin[29]. In contrast, the distal site uses an entirely different interface on both ankyrin and the band 3 cytoplasmic domain, and is further stabilized by interactions of the N-terminal peptide of band 3 with the peptide binding groove of ankyrin.

Monomeric GPA binds to the band 3 dimer. One GPA monomer binds to each band 3 protomer, with the GPA transmembrane helix packing with TM3 and TM4 of band 3, and the extracellular N-terminal extension interacting with the TM7-8 loop, which includes E658, the critical residue for formation of the Wright blood group antigen[30]. H85 of GPA appears to be forming a salt bridge with E658, likely representing the interaction that is variously present and absent in the different Wright blood types. This had previously been proposed to originate from a salt bridge with R61 of GPA[30], which is disordered in our structure. A cholesterol-mediated interaction with TM8 of band 3 is also observed, consistent with the known importance of TM8 in the band 3–GPA interaction[31]. Only monomeric GPA is observed binding to band 3, despite the known propensity of GPA to dimerize. This is consistent with studies showing that mutations that inhibit GPA dimerization do not inhibit band 3 dependent effects of GPA[32], but still leaves a puzzle: why does the GPA dimer not interact with band 3? Structural alignment of the crystal structure of the GPA dimer[33] with band 3-bound GPA shows that the second molecule of GPA would have to be embedded entirely within the membrane, in an almost horizontal orientation, which is highly energetically unfavorable. We speculate that in the membrane, GPA exists in a monomer–dimer equilibrium and band 3 selectively binds monomeric GPA. In the context of the Class 1 model of the ankyrin-1 complex, the GPA molecules bound to Band 3-II and Band 3-III are in close proximity, although we cannot be certain they are interacting. The possibility of GPA mediating end-to-end attachment of two band 3 dimers would be consistent with both previous molecular dynamics simulations of band 3 in the presence of modeled GPA[34], as well as the known propensity of detergent-solubilized band 3 purified from erythrocytes to form 'tetramers' in solution[35].

Protein 4.2 facilitates recruitment of Band 3-I and AQP1. The structure of the ankyrin-1 complex also establishes a role for protein 4.2, a highly abundant component of the erythrocyte. Protein 4.2 is known to interact with both band 3 and ankyrin[36], but the implication of these interactions was unclear. We observe that protein 4.2 plays a role as an adaptor, stabilizing the interaction of ankyrin with the membrane and facilitating recruitment of an additional dimer of the band 3 anion exchanger (Band 3-I) via interactions with both the cytoplasmic and TM regions, the latter of which appears to be at least partially mediated by a PIP_2 lipid bound at the band 3 transmembrane dimer interface. Furthermore, protein 4.2 appears to play an additional role in facilitating the recruitment of AQP1, the C terminus of which directly interacts with domain 1 of protein 4.2.

Aquaporin-1 is a component of the ankyrin-1 complex. The identification of aquaporin-1 as a component of the ankyrin-1 complex (Fig. 4) was an unexpected finding, although consistent with fluorescence resonance energy transfer measurements indicating that AQP1 is located within 8 nm of band 3 dimers[37]. The observation

that AQP1 expression is decreased, and glycosylation pattern altered in both murine and human erythrocytes lacking band 3 (ref. [24]) is also compatible with a role for AQP1 in the ankyrin-1 complex. It has been proposed that the cluster of membrane proteins that ankyrin-1 organizes in the red blood cell (RBC) membrane forms a CO_2 metabolon[38], linking facilitated diffusion of CO_2 across the membrane, anion exchange of Cl^-/HCO_3^- via band 3, and interconversion of dissolved CO_2 and carbonic acid in the cytosol via carbonic anhydrase, which binds to the C-terminal tail of band 3 (ref. [39]) and catalyzes conversion of CO_2 and H_2O to HCO_3^- and H^+. A role for AQP1 in the CO_2 metabolon would be consistent with the known capacity of AQP1 to conduct both CO_2 and H_2O (ref. [40]), both of which are substrates for carbonic anhydrase. RhAG may also participate indirectly in this process, by allowing facilitated diffusion of NH_3 and consequent modulation of $[H^+]$, via the equilibrium of $NH_3 + H^+$ and NH_4^+.

RhCE recruits ankyrin-1 to the membrane. The heterotrimeric Rh ammonia channel plays an important role in ammonium homeostasis in the blood[41], and in maintaining the stability of the RBC membrane[12]. Humans express five Rh family proteins—RhAG, RhCE and RhD in erythrocytes, and RhBG and RhCG in the kidney epithelium. The structure of the RhCG homotrimer[42] showed that the eukaryotic Rh family shares a great deal of similarity to the bacterial AmtB family of ammonium transporters, including a conserved twin-histidine motif in the central pore. It has been suggested that RhAG mediates ammonia or possibly carbon dioxide transport[43,44] across the erythrocyte membrane[45]. The functional role of RhCE and RhD in the structure and function of the RBC membrane has been much debated, as has the stoichiometry of the heterotrimeric Rh complex. The 2.2 Å resolution structure of the $(RhAG)_2RhCE$ heterotrimer (Fig. 5a,b) in the context of the ankyrin-1 complex resolves the stoichiometry question, and suggests that the primary role of RhCE might be as a recruitment site for ankyrin-1, via binding of the N and C termini to AR1-5 of ankyrin-1. Other putative roles for RhCE remain speculative. It has been proposed, based on homology modeling[46] and the absence in RhCE/D of the characteristic twin-histidine motif, that RhCE and RhD lack a membrane transport function completely. Our work, while not conclusively demonstrating that RhCE retains a transport function, shows that RhCE has a pore that extends almost completely across the membrane, impeded by only by a small cluster of hydrophobic residues and that it seems to be more dynamic than RhAG. We therefore suggest that the possibility of an auxiliary transport function for RhCE in the erythrocyte membrane may be worth investigating.

Concluding remarks. In summary, we have reported the structure of an erythrocyte ankyrin-1 complex, purified from human erythrocytes. We have structurally characterized two direct binding sites for the band 3 anion exchanger on ankyrin-1, as well as one band 3 binding site mediated by protein 4.2, identified aquaporin-1 as a component of the complex, determined the stoichiometry of the heterotrimeric Rhesus ammonia channel and identified RhCE as the ankyrin-1 binding subunit of the Rhesus channel. Taken together these findings offer insights into the molecular architecture of the RBC membrane, and show how ankyrins can facilitate the simultaneous recruitment of multiple classes of membrane proteins, to enable functional organization of membrane transport processes.

Online content

Any methods, additional references, Nature Research reporting summaries, source data, extended data, supplementary information, acknowledgements, peer review information; details of author contributions and competing interests; and statements of data and code availability are available at https://doi.org/10.1038/s41594-022-00792-w.

Received: 22 December 2021; Accepted: 24 May 2022;
Published online: 14 July 2022

References

1. Marchesi, V. T. & Steers, E. Selective solubilization of a protein component of the red cell membrane. *Science* **159**, 203–204 (1968).
2. Unsain, N., Stefani, F. D. & Cáceres, A. The actin/spectrin membrane-associated periodic skeleton in neurons. *Front. Synaptic Neurosci.* https://doi.org/10.3389/fnsyn.2018.00010 (2018).
3. Bennett, V. & Stenbuck, P. J. Identification and partial purification of ankyrin, the high affinity membrane attachment site for human erythrocyte spectrin. *J. Biol. Chem.* **254**, 2533–2541 (1979).
4. Bennett, V. & Stenbuck, P. J. The membrane attachment protein for spectrin is associated with band 3 in human erythrocyte membranes. *Nature* **280**, 468–473 (1979).
5. Stevens, S. R. et al. Ankyrin-R regulates fast-spiking interneuron excitability through perineuronal nets and Kv3.1b K^+ channels. *eLife* **10**, e66491 (2021).
6. Mohler, P. J., Davis, J. Q. & Bennett, V. Ankyrin-B coordinates the Na/K ATPase, Na/Ca exchanger, and InsP3 receptor in a cardiac T-tubule/SR microdomain. *PLoS Biol.* **3**, e423 (2005).
7. Jenkins, P. M. et al. Giant ankyrin-G: a critical innovation in vertebrate evolution of fast and integrated neuronal signaling. *Proc. Natl Acad. Sci. USA* **112**, 957–964 (2015).
8. Jenkins, S. M. & Bennett, V. Ankyrin-G coordinates assembly of the spectrin-based membrane skeleton, voltage-gated sodium channels, and L1 CAMs at Purkinje neuron initial segments. *J. Cell Biol.* **155**, 739–746 (2001).
9. Bennett, V. Purification of an active proteolytic fragment of the membrane attachment site for human erythrocyte spectrin. *J. Biol. Chem.* **253**, 2292–2299 (1978).
10. Perrotta, S., Gallagher, P. G. & Mohandas, N. Hereditary spherocytosis. *Lancet* **372**, 1411–1426 (2008).
11. Bennett, V. & Healy, J. Organizing the fluid membrane bilayer: diseases linked to spectrin and ankyrin. *Trends Mol. Med.* **14**, 28–36 (2008).
12. Nicolas, V. et al. Rh-RhAG/ankyrin-R, a new interaction site between the membrane bilayer and the red cell skeleton, is impaired by Rh(null)-associated mutation. *J. Biol. Chem.* **278**, 25526–25533 (2003).
13. Jiang, W. et al. Interaction of glucose transporter 1 with anion exchanger 1 in vitro. *Biochem. Biophys. Res. Commun.* **339**, 1255–1261 (2006).
14. Mankelow, T. J., Satchwell, T. J. & Burton, N. M. Refined views of multi-protein complexes in the erythrocyte membrane. *Blood Cells Mol. Dis.* **49**, 1–10 (2012).
15. Young, G. et al. Quantitative mass imaging of single biological macromolecules. *Science* **360**, 423–427 (2018).
16. Bepler, T. et al. Positive-unlabeled convolutional neural networks for particle picking in cryo-electron micrographs. *Nat. Methods* **16**, 1153–1160 (2019).
17. Chen, K., Li, J., Wang, C., Wei, Z. & Zhang, M. Autoinhibition of ankyrin-B/G membrane target bindings by intrinsically disordered segments from the tail regions. *eLife* **6**, e29150 (2017).
18. Wang, C. et al. Structural basis of diverse membrane target recognitions by ankyrins. *eLife* https://doi.org/10.7554/eLife.04353 (2014).
19. Toye, A. M. et al. Protein-4.2 association with band 3 (AE1, SLCA4) in Xenopus oocytes: effects of three natural protein-4.2 mutations associated with hemolytic anemia. *Blood* **105**, 4088–4095 (2005).
20. Satchwell, T. J., Shoemark, D. K., Sessions, R. B. & Toye, A. M. Protein 4.2: a complex linker. *Blood Cells Mol. Dis.* **42**, 201–210 (2009).
21. Risinger, M. A., Dotimas, E. M. & Cohen, C. M. Human erythrocyte protein 4.2, a high copy number membrane protein, is N-myristylated. *J. Biol. Chem.* **267**, 5680–5685 (1992).
22. Beckmann, R., Smythe, J. S., Anstee, D. J. & Tanner, M. J. Coexpression of band 3 mutants and Rh polypeptides: differential effects of band 3 on the expression of the Rh complex containing D polypeptide and the Rh complex containing CcEe polypeptide. *Blood* **97**, 2496–2505 (2001).
23. Hanicak, A. et al. Erythrocyte band 3 protein strongly interacts with phosphoinositides. *FEBS Lett.* **348**, 169–172 (1994).
24. Bruce, L. J. et al. A band 3-based macrocomplex of integral and peripheral proteins in the RBC membrane. *Blood* **101**, 4180–4188 (2003).
25. Perrotta, S. et al. The N-terminal 11 amino acids of human erythrocyte band 3 are critical for aldolase binding and protein phosphorylation: implications for band 3 function. *Blood* **106**, 4359–4366 (2005).
26. Ferru, E. et al. Regulation of membrane-cytoskeletal interactions by tyrosine phosphorylation of erythrocyte band 3. *Blood* **117**, 5998–6006 (2011).
27. Ding, Y., Casey, J. R. & Kopito, R. R. The major kidney AE1 isoform does not bind ankyrin (Ank1) in vitro. An essential role for the 79 NH_2-terminal amino acid residues of band 3. *J. Biol. Chem.* **269**, 32201–32208 (1994).
28. Kim, S. et al. Determination of structural models of the complex between the cytoplasmic domain of erythrocyte band 3 and ankyrin-R repeats 13-24. *J. Biol. Chem.* **286**, 20746–20757 (2011).

29. Chang, S. H. & Low, P. S. Identification of a critical ankyrin-binding loop on the cytoplasmic domain of erythrocyte membrane band 3 by crystal structure analysis and site-directed mutagenesis. *J. Biol. Chem.* **278**, 6879–6884 (2003).
30. Bruce, L. J. et al. Changes in the blood group Wright antigens are associated with a mutation at amino acid 658 in human erythrocyte band 3: a site of interaction between band 3 and glycophorin A under certain conditions. *Blood* **85**, 541–547 (1995).
31. Williamson, R. C. & Toye, A. M. Glycophorin A: band 3 aid. *Blood Cells Mol. Dis.* **41**, 35–43 (2008).
32. Young, M. T., Beckmann, R., Toye, A. M. & Tanner, M. J. Red-cell glycophorin A-band 3 interactions associated with the movement of band 3 to the cell surface. *Biochem. J.* **350 Pt 1**, 53–60 (2000).
33. Trenker, R., Call, M. E. & Call, M. J. Crystal structure of the glycophorin A transmembrane dimer in lipidic cubic phase. *J. Am. Chem. Soc.* **137**, 15676–15679 (2015).
34. Kalli, A. C. & Reithmeier, R. A. F. Interaction of the human erythrocyte Band 3 anion exchanger 1 (AE1, SLC4A1) with lipids and glycophorin A: molecular organization of the Wright (Wr) blood group antigen. *PLoS Comput. Biol.* **14**, e1006284 (2018).
35. Taylor, A. M., Boulter, J., Harding, S. E., Cölfen, H. & Watts, A. Hydrodynamic properties of human erythrocyte band 3 solubilized in reduced Triton X-100. *Biophys. J.* **76**, 2043–2055 (1999).
36. Su, Y. et al. Associations of protein 4.2 with band 3 and ankyrin. *Mol. Cell Biochem.* **289**, 159–166 (2006).
37. Hsu, K. et al. Adaptable interaction between aquaporin-1 and band 3 reveals a potential role of water channel in blood CO2 transport. *FASEB J.* **31**, 4256–4264 (2017).
38. Reithmeier, R. A. A membrane metabolon linking carbonic anhydrase with chloride/bicarbonate anion exchangers. *Blood Cells Mol. Dis.* **27**, 85–89 (2001).
39. Vince, J. W. & Reithmeier, R. A. Carbonic anhydrase II binds to the carboxyl terminus of human band 3, the erythrocyte C1-/HCO3- exchanger. *J. Biol. Chem.* **273**, 28430–28437 (1998).
40. Endeward, V. et al. Evidence that aquaporin 1 is a major pathway for CO2 transport across the human erythrocyte membrane. *FASEB J.* **20**, 1974–1981 (2006).
41. Planelles, G. Ammonium homeostasis and human Rhesus glycoproteins. *Nephron Physiol.* **105**, p11–p17 (2007).
42. Gruswitz, F. et al. Function of human Rh based on structure of RhCG at 2.1 A. *Proc. Natl Acad. Sci. USA* **107**, 9638–9643 (2010).
43. Geyer, R. R., Parker, M. D., Toye, A. M., Boron, W. F. & Musa-Aziz, R. Relative CO_2/NH_3 permeabilities of human RhAG, RhBG and RhCG. *J. Membr. Biol.* **246**, 915–926 (2013).
44. Endeward, V., Cartron, J. & Ripoche, P., Gros, and G. RhAG protein of the Rhesus complex is a CO_2 channel in the human red cell membrane. *FASEB J.* **22**, 64–73 (2008).
45. Burton, N. M. & Anstee, D. J. Structure, function and significance of Rh proteins in red cells. *Curr. Opin. Hematol.* **15**, 625–630 (2008).
46. Conroy, M. J., Bullough, P. A., Merrick, M. & Avent, N. D. Modelling the human rhesus proteins: implications for structure and function. *Br. J. Haematol.* **131**, 543–551 (2005).

Methods

Preparation of erythrocyte ghost membranes. Ghost membranes were prepared as described in Niggli et al.[47]. Briefly, RBCs from healthy blood donors were provided by the Transfusion Center of the Hospital of Padua (Italy). Samples were obtained from voluntary and informed blood donation for transfusions. Erythrocytes from fresh human blood samples were washed twice in 5 volumes of 130 mM KCl and 10 mM Tris-HCl, pH 7.4. The cells were hemolyzed in 5 volumes of 1 mM EDTA and 10 mM Tris-HCl, pH 7.4, and centrifuged at 18,000*g* for 10 min. The ghost membranes were then washed five times in the hemolysis buffer, and four additional times in 10 mM HEPES, pH 7.4. The hemoglobin-free ghost membranes were finally resuspended in 130 mM NaCl, 20 mM HEPES, pH 7.4, 0.5 mM $MgCl_2$, 0.05 mM $CaCl_2$ and 2 mM DTT, and stored at −80 °C.

Purification of the erythrocyte ankyrin-1 complex. The general purification workflow is presented in Supplementary Fig 1. Ghost membranes were solubilized at a protein concentration of 4 mg ml^{-1} in 130 mM KCl and 10 mM HEPES, pH 7.4, protease inhibitor tablet (cOmplete, EDTA-free Protease Inhibitor Cocktail, Millipore Sigma), 1% (w/v) digitonin (Carbosynth), 1 mM ATP, 1 mM $MgCl_2$ and 1 mM PMSF, at 4 °C for 1 h. Unsolubilized material was removed by centrifugation at 26,000*g* for 30 min. The supernatant was applied to a PD10 column (to reduce the detergent concentration) equilibrated with 0.05% (w/v) digitonin, 130 mM KCl, 20 mM HEPES, pH 7.4, 1 mM ATP, 1 mM $MgCl_2$ and 1 mM PMSF. The sample was than applied on a glycerol step gradient (30–12% glycerol) and centrifuged for 15 h at 25,000 r.p.m. (SW 32 rotor, Beckman). The separation and distribution of proteins was confirmed by SDS–PAGE gel (4–20% Mini-PROTEAN TGX Precast Protein Gels, Biorad). Fractions containing high molecular weight species were pooled together and concentrated to <500 µl using a 100-kDa cutoff concentrator. The sample was loaded on a Superose 6 10/300 Increase column (Cytiva) equilibrated in 0.05% (w/v) digitonin, 130 mM KCl, 20 mM HEPES, pH 7.4, 1 mM ATP, 1 mM $MgCl_2$ and 1 mM PMSF. Fractions of a peak around an 11 ml elution volume were analyzed using a mass photometer (Refeyn OneMP), pooled and concentrated to 8 mg ml^{-1}.

Vesicle preparation. Ghost membranes (roughly 100 mg) were pelleted (6,000*g*, 10 min), washed five times in 130 mM KCl and 10 mM HEPES, pH 7.4 and then homogenized with the same buffer. The sample was sonicated using microprobe (amplitude 30, pulse on 5 s, rest time 10 s, total pulse on 50 s). Large fragments are removed by centrifugation (6,000*g*, 10 min) and the supernatant was extruded (Avanti Polar Lipid) ten times using a 400 nm filter. After extrusion, vesicles were collected by ultra-centrifugation at 35,000 r.p.m. for 30 min (S120-AT3, Sorvall). The pellet, which contains vesicles, was resuspended at a final concentration of 5 mg ml^{-1}. All steps were performed at room temperature to facilitate vesicle formation.

Mass photometry (iSCAMS). Mass photometry experiments were performed using a Refeyn OneMP (Refeyn Ltd). Data acquisition was accomplished using AcquireMP (Refeyn Ltd 172 v.2.3). Samples were evaluated with microscope coverslips. The coverslips (cover glass thickness 1.5 24 × 50 mm, Corning) were washed with ddH_2O and isopropanol. Silicone templates were placed on top of the coverslip to form reaction chambers immediately before measurement. The instrument was calibrated using NativeMark Protein Standards (NativeMark Unstained Protein Standard, ThermoFisher). Then 10 µl of fresh room temperature buffer was pipetted into a well, the focal position was identified and locked. For each acquisition, 1 µl of the protein (at a final concentration after dilution of 200 nM) was added to the well and thoroughly mixed. Mass photometry signals were recorded for 60 s to allow detection of at least 2×10^3 individual binding events. Data analysis was carried out using the DiscoverMP software.

Cryo-EM and Cryo-ET grid preparation and data collection. Here, 3 µl of purified ankyrin complex at 8 mg ml^{-1}, with a surface-active additive (0.01% (w/v) glycyrrhizic acid) was added to a glow discharged (PELCO easiGlow) holey gold grid (Quantifoil UltrAuFoil grids (R0.6/1, Au 300-mesh gold)) and blotted for 4 to 6 s at 4 °C and 100% humidity using the Vitrobot system (ThermoFisher), before plunging immediately into liquid ethane for vitrification. Images were collected on a Titan Krios electron microscope (FEI) equipped with a K3 direct electron detector (Gatan) operating at 0.83 Å per pixel in counting mode using Leginon automated data collection software. Data collection was performed using a dose of 58 $e^-/Å^2$ across 50 frames (50 ms per frame) at a dose rate of 16 e^- pixel^{-1} s^{-1}, using a set defocus range of −0.5 to −1.5 µm. A 100-µm objective aperture was used. A total of 14,464 micrographs were collected.

Vesicles for cryo-ET were prepared similarly using 1.2/1.3-µm holey gold grids (Quantifoil UltrAuFoil) and blotted for 10 s using a Vitrobot Mark IV (ThermoFisher), before plunging immediately into liquid ethane for vitrification. About 100 tilt series were collected on a Titan Krios electron microscope (FEI) equipped with a K3 direct electron detector (Gatan), energy filter (Gatan) and Cs-corrector, operating at 2.077 Å per pixel in counting mode using Leginon automated data collection software[48]. Tilt series were collected bidirectionally from [0:+51]° then [0:−51]° in 3° increments, with a dose of 3.13 $e^-/Å^2$ across eight frames (57 ms per frame) total dose of 112 $e^-/Å^2$ across 36 total images per tilt series, using a nominal defocus range of −3.5 to −4.5 µm.

Cryo-EM data processing. The final cryo-EM data processing workflow is summarized in Supplementary Fig. 3. Orientation distributions, Fourier shell correlation (FSC) plots and validation statistics are presented in Extended Data Fig. 1c and Table 1. Maps, masks and raw videos have been deposited at EMDB (Table 1) and EMPIAR (IDs EMPIAR-11043). Subsequent steps were performed in cryoSPARC v.3.2–v.3.3 unless otherwise indicated[49].

Motion correction, contrast transfer function (CTF) estimation and micrograph curation. Patch-based motion correction and dose weighting of 14,464 cryo-EM videos was carried out in cryoSPARC using the Patch Motion job type. Patch-based CTF estimation was performed on the aligned averages using Patch CTF.

Particle picking. An initial round of exploratory processing was performed using Blob Picker. Ranking the micrographs by the number of particles remaining after 2D classification, 58 exemplary micrographs were selected for manual picking to create a training dataset for the Topaz neural network-based picker[16]. Then 1,510 particles corresponding to large complexes were manually picked from 58 micrographs. Topaz was run in training mode using a downsampling factor of 6 and an estimated number of particles per micrograph of 200. The resulting model was used to pick particles using Topaz Extract. Initially, 1.8 million particles were extracted in a box of 600 pixels and Fourier cropped to 150 pixels for initial cleanup (2D and initial 3D classification).

2D classification. Multiple rounds of 2D classification were performed to isolate homogeneous subsets of particles to use for ab initio reconstruction of compositionally distinct classes. The 48 most occupied 2D classes from the initial round of 2D classification are presented in Extended Data Fig. 1b.

Initial model generation. Heterogeneous ab initio reconstruction was performed on a variety of subsets of particles selected by 2D classification, to generate a diverse range of initial models representing distinct 3D classes in the data for further classification.

Initial 3D classification. Heterogeneous refinement was performed using the Topaz picked initial particle stack of 1.8 million particles, with 12 representative initial reconstructions as map inputs. Four well-defined, high-resolution classes of the ankyrin complex were identified, as well as several well-defined classes of smaller particles, most of which were identified as free band 3 dimers. Then 710,000 particles corresponding to ankyrin complexes were re-extracted with recentering in a 450 pixel box.

Consensus refinement. An initial refinement of all 710,000 ankyrin complex particles was performed using nonuniform refinement with on-the-fly refinement of per particle defocus, and global refinement of beam tilt and trefoil aberrations, giving an initial consensus refinement with a resolution of 2.3 Å. The use of dynamic masking and real-space windowing of particle images during refinement was disabled. Masked refinements of the Rh trimer, ankyrin-1 membrane binding domain, protein 4.2, the cytoplasmic domains of Band 3-I and the transmembrane domains of Band 3-I were performed starting from the global consensus refinement with local angular searches.

Subclassification of ankyrin complex particles. Based on subclassification of each of the original four classes, six nonredundant classes were identified. The 710,000 stack of clean ankyrin complex particles from the consensus refinement was subjected to heterogenous refinement using these six classes as inputs, as well as five decoy classes, using an initial low-pass filter of 50 Å and a batch size per class of 5,000 particles. The composition and occupancy of the resulting classes is summarized in Supplementary Fig. 5.

Subclassification using 3D-variability analysis. In the case of Band 3-I, Band 3-II, Band 3-III and AQP1, another approach was taken to isolate a set of particles with improved density for the mobile component (Extended Data Fig. 6). First, a local refinement with a mask around the mobile component was performed, yielding a relatively poor resolution, noisy local reconstruction (3.8 Å in the case of Band 3-I starting from the consensus refinement). Then, 3D-variability analysis was carried out as implemented in cryoSPARC 3.2, selecting five modes, with a filter resolution of 3–4.5 Å. Reconstructions were calculated along each mode, and a mode corresponding to an order–disorder transition of the mobile subregion was identified. This mode was then used (using the 3D Variability Analysis Display job type) to split the particles into 20 clusters, and a reconstruction calculated for each. Particles belonging to clusters with well-defined, high-resolution features were combined, realigned globally by nonuniform refinement and subjected to another round of local refinement, In the case of Band 3-I local refinement from the consensus refinement of all ankyrin-1 complexes, this yielded a map with a resolution of 2.8 Å.

Processing of free band 3–GPA dimer particles. In a separate processing pathway, after identification of the free band 3 dimer class using multi class ab initio reconstruction, several successive rounds of heterogeneous refinement were

performed using a single band 3 dimer class and eight random density decoys, against the original 1.8 million particle stack. This allowed isolation of a subset of 37,000 particles that were re-extracted in a 320 pixel box and refined with nonuniform regularization to obtain a reconstruction at 2.8 Å resolution. Training a Topaz model and repicking the dataset with a model biased toward band 3–GPA dimer particles provided a substantial increase in the number of high-quality particles, and resulted in a 2.3 Å reconstruction from 166,000 particles.

Local refinements and generation of composite maps. For the consensus refinement, class 1 and class 2, local refinements using several different masks were performed to generate local reconstructions with improved density. Maps were post-processed by density modification, soft masking outside the refinement mask and cropping to a minimal box using phenix.resolve_cryo_em (without using an atomic model in the analysis) and resampled to 0.415 Å per pixel using relion_image_handler to best visualize high-resolution structural details. For deposition of each local refinement, the density modified, cropped and resampled map has been designated as the main map, with nondensity modified half maps that have been cropped and resampled to match the map used for model building. Raw half maps, and an optimally *B* factor sharpened full reconstruction, are provided as additional maps for each deposition. To aid model building of the complex, composite maps of the consensus (all classes combined), Classes 1 and 2 were generated by aligning all the relevant local maps to the matching global reconstruction, and then combining them by taking the maximum value at each voxel using UCSF Chimera[50]. Composite maps were created from both the density modified maps, and the unsharpened, unmasked local maps, and both have been provided in each composite map deposition, along with the global reconstruction (and matching half maps) as additional maps.

Cryo-EM data validation. Map resolution was estimated using the gold-standard FSC = 0.143 criterion, calculated from half maps using a soft mask in Relion v.3.1 (ref. [51]). Detailed validation statistics are provided in Table 1.

Atomic model building and refinement. An initial model for protein 4.2 was generated using trROSETTA[52]. Ankyrin-1 (ref. [53]) (Protein Data Bank (PDB) ID 1N11), Band 3 (refs. [54,55]) (PDB IDs 4YZF and 1HYN) and aquaporin crystal structures[56] (PDB 4CSK) were used as initial models for building the corresponding proteins. Initial models for RhCE and RhAG were generated by threading using CHAINSAW[57] as implemented in the CCP4 package[58], using the structure of the RhCG homotrimer as a template[42] (PDB 3HD6). Initial models were placed in corresponding local refinements and and fit as rigid bodies using UCSF Chimera[50]. Each submodel was then manually extended and completed in COOT[59–61], waters and ligands were added where justified by the density and chemical environment, and each final model was refined against the local map using phenix.real_space_refine[62]. Finally, models were fit to the composite map, merged, then flexibly fit using phenix.real_space_refine. The combined model of class 1a was rigid body fit to the ankyrin-1 complex subtomogram average, after which ligands, waters and side chains were stripped, leaving a polyalanine model. Figures were prepared using UCSF ChimeraX[63]. Refinement and validation statistics are provided in Table 1.

Cryo-ET data processing. Tilt images were frame aligned with MotionCor2 (ref. [64]) without patches or dose weighting. Frame aligned tilt images were used for fiducial-less tilt-series alignment in Appion-Protomo[65–67]. Aligned tilt series were dose weighted in Appion-Protomo using equation 3 in Grant and Grigorieff[68] reconstructed for initial visualization with Tomo3D (refs. [69,70]) SIRT and separately without dose weighting with Warp[71]. Seven binned by four Warp tomograms (pixel size 8.308 Å) were used to train an IsoNet[72] model (where 300 subtomograms were extracted at 963 voxels after masking with *z* axis cropping to remove void volumes, then trained over 35 iterations), which was then applied to each tomogram for visualization with IMOD[73].

Cryo-ET subtomogram averaging. Tilt images were frame aligned with MotionCor2 (ref. [64]) without patches or dose weighting. The unaligned tilt images were imported into Warp[71] after CTF preprocessing using Warp from the frames. The tilt series were aligned with AreTomo[74] and the alignment files were imported back into Warp, where CTF correction was performed. Tilt series that had poorly modeled CTFs were manually removed. Tomogram reconstruction was performed in Warp at 8.308 Å per pixel. The missing wedge was corrected using IsoNet (as described above) to enhance visualization for particle picking. Twenty missing wedge corrected tomograms were manually picked with crYOLO[75] to obtain 10,000 particle coordinates. The particle coordinates were used to train crYOLO on uncorrected tomograms. Prediction was performed on 60 tomograms where a total of 60,029 particles were obtained. The particles were extracted in Warp at 4 Å per pixel with a box size of 80 pixels. Initial models were generated in Relion v.4 using stochastic gradient descent, with eight classes requested. The resulting initial map that most closely resembled the ankyrin-1 complex was low-pass filtered to 60 Å and used for multiple rounds of 3D classification in Relion v.4 (refs. [76,77]) with a spherical mask of 300 Å at an angular sampling interval of 7.5°. After 3D classification, 1,596 particles were re-extracted in a 140 pixel box and used for refinement in Relion v.4 with a soft spherical mask, giving a final map with a nominal resolution of 25 Å.

Reporting summary. Further information on research design is available in the Nature Research Reporting Summary linked to this article.

Data availability

All raw video files, aligned micrographs and particle coordinates (in two STAR files, one for band 3–GPA and one for the ankyrin complexes) are deposited in the EMPIAR (EMPIAR-11043). The cryo-EM density maps and models have been deposited in the Electron Microscopy Data Bank and the PDB. PDB IDs are: 7UZ3, 7UZE, 7UZQ, 7UZS, 7UZU, 7UZV, 7V07, 7V0K, 7V0M, 7V0Q, 7V0S, 7V0T, 7V0U, 7V0X, 7V0Y, 7V19, 8CRQ, 8CRR, 8CRT, 8CS9, 8CSV, 8CSW, 8CSX, 8CSY, 8CT2, 8CT3, 8CSL and 8CTE. EMDB IDs are: EMD-26874, EMD-26886, EMD-26916, EMD-26917, EMD-26918, EMD-26919, EMD-26940, EMD-26943, EMD-26944, EMD-26948, EMD-26949, EMD-26950, EMD-26951, EMD-26952, EMD-26953, EMD-26954, EMD-26955, EMD-26956, EMD-26958, EMD-26960, EMD-26972, EMD-26973, EMD-26974, EMD-26975, EMD-26978, EMD-26979, EMD-26982, EMD-26965 and EMD-26988.

References

47. Niggli, V. & Carafoli, E. The plasma membrane Ca(2+) ATPase: purification by calmodulin affinity chromatography, and reconstitution of the purified protein. *Methods Mol. Biol.* **1377**, 57–70 (2016).
48. Suloway, C. et al. Fully automated, sequential tilt-series acquisition with Leginon. *J. Struct. Biol.* **167**, 11–18 (2009).
49. Punjani, A., Rubinstein, J. L., Fleet, D. J. & Brubaker, M. A. cryoSPARC: algorithms for rapid unsupervised cryo-EM structure determination. *Nat. Methods* **14**, 290–296 (2017).
50. Pettersen, E. F. et al. UCSF Chimera–a visualization system for exploratory research and analysis. *J. Comput. Chem.* **25**, 1605–1612 (2004).
51. Zivanov, J. et al. New tools for automated high-resolution cryo-EM structure determination in RELION-3. *eLife* **7**, e42166 (2018).
52. Yang, J. et al. Improved protein structure prediction using predicted interresidue orientations. *Proc. Natl Acad. Sci. USA* **117**, 1496–1503 (2020).
53. Michaely, P., Tomchick, D. R., Machius, M. & Anderson, R. G. W. Crystal structure of a 12 ANK repeat stack from human ankyrinR. *EMBO J.* **21**, 6387–6396 (2002).
54. Arakawa, T. et al. Crystal structure of the anion exchanger domain of human erythrocyte band 3. *Science* **350**, 680–684 (2015).
55. Zhang, D., Kiyatkin, A., Bolin, J. T. & Low, P. S. Crystallographic structure and functional interpretation of the cytoplasmic domain of erythrocyte membrane band 3. *Blood* **96**, 2925–2933 (2000).
56. Ruiz Carrillo, D. et al. Crystallization and preliminary crystallographic analysis of human aquaporin 1 at a resolution of 3.28Å. *Acta Crystallogr. F. Struct. Biol. Commun.* **70**, 1657–1663 (2014).
57. Stein, N. CHAINSAW: a program for mutating PDB files used as templates in molecular replacement. *J. Appl. Crystallogr.* **41**, 641–643 (2008).
58. Winn, M. D. et al. Overview of the *CCP* 4 suite and current developments. *Acta Crystallogr. D. Biol. Crystallogr.* **67**, 235–242 (2011).
59. Emsley, P., Lohkamp, B., Scott, W. G. & Cowtan, K. Features and development of Coot. *Acta Crystallogr. D. Biol. Crystallogr.* **66**, 486–501 (2010).
60. Emsley, P. & Cowtan, K. Coot: model-building tools for molecular graphics. *Acta Crystallogr. D. Biol. Crystallogr.* **60**, 2126–2132 (2004).
61. Casañal, A., Lohkamp, B. & Emsley, P. Current developments in Coot for macromolecular model building of electron cryo-microscopy and crystallographic data. *Protein Sci.* **29**, 1069–1078 (2020).
62. Afonine, P. V. et al. Real-space refinement in PHENIX for cryo-EM and crystallography. *Acta Crystallogr. D. Struct. Biol.* **74**, 531–544 (2018).
63. Pettersen, E. F. et al. UCSF ChimeraX: structure visualization for researchers, educators, and developers. *Protein Sci.* **30**, 70–82 (2021).
64. Zheng, S. Q. et al. MotionCor2: anisotropic correction of beam-induced motion for improved cryo-electron microscopy. *Nat. Methods* **14**, 331–332 (2017).
65. Noble, A. J. & Stagg, S. M. Automated batch fiducial-less tilt-series alignment in Appion using Protomo. *J. Struct. Biol.* **192**, 270–278 (2015).
66. Winkler, H. & Taylor, K. A. Accurate marker-free alignment with simultaneous geometry determination and reconstruction of tilt series in electron tomography. *Ultramicroscopy* **106**, 240–254 (2006).
67. Lander, G. C. et al. Appion: an integrated, database-driven pipeline to facilitate EM image processing. *J. Struct. Biol.* **166**, 95–102 (2009).
68. Grant, T. & Grigorieff, N. Measuring the optimal exposure for single particle cryo-EM using a 2.6Å reconstruction of rotavirus VP6. *eLife* **4**, e06980 (2015).
69. Agulleiro, J. I. & Fernandez, J. J. Fast tomographic reconstruction on multicore computers. *Bioinformatics* **27**, 582–583 (2011).

70. Agulleiro, J.-I. & Fernandez, J.-J. Tomo3D 2.0 – exploitation of advanced vector extensions (AVX) for 3D reconstruction. *J. Struct. Biol.* **189**, 147–152 (2015).
71. Tegunov, D. & Cramer, P. Real-time cryo-electron microscopy data preprocessing with Warp. *Nat. Methods* **16**, 1146–1152 (2019).
72. Liu, Y.-T. et al. Isotropic reconstruction of electron tomograms with deep learning. Preprint at *bioRxiv* https://doi.org/10.1101/2021.07.17.452128 (2021).
73. Kremer, J. R., Mastronarde, D. N. & McIntosh, J. R. Computer visualization of three-dimensional image data using IMOD. *J. Struct. Biol.* **116**, 71–76 (1996).
74. Zheng, S. et al. AreTomo: an integrated software package for automated marker-free, motion-corrected cryo-electron tomographic alignment and reconstruction. *J. Struct. Biol. X* **6**, 100068 (2022).
75. Wagner, T. et al. SPHIRE-crYOLO is a fast and accurate fully automated particle picker for cryo-EM. *Commun. Biol.* **2**, 218 (2019).
76. Zivanov, J. et al. A Bayesian approach to single-particle electron cryo-tomography in RELION-4.0. Preprint at *bioRxiv* https://doi.org/10.1101/2022.02.28.482229 (2022).
77. Kimanius, D., Dong, L., Sharov, G., Nakane, T. & Scheres, S. H. W. New tools for automated cryo-EM single-particle analysis in RELION-4.0. *Biochem. J.* **478**, 4169–4185 (2021).

Acknowledgements

Cryo-EM data were collected at Columbia Cryo-EM facility and at the Simons Electron Microscopy Center (SEMC), directed by B. Carragher and C. Potter, with the assistance of staff from both SEMC and the Columbia University Cryo-Electron Microscopy Center. R. Grassucci and Z. Zhang from the Columbia Cryo-EM Center assisted with data collection. Some of the work was performed using equipment from the Center for Membrane Protein Production and Analysis (COMPPÅ; grant no. NIH P41 GM116799 to W.A. Hendrickson). We thank L. Maso for generating the schematic representation of the ankyrin-1 complex (Fig. 1c) and F. Mancia and his laboratory members for support and critical reading of the manuscript. We thank G. Gillis for assisting during protein purification. We are grateful to P. Berto and L. Barazzuol, Department of Biomedical Sciences, University of Padova, for their support in the preparation of the ghost membranes. We thank the 'Centro Transfusionale dell'Azienda Ospedaliera Università di Padova' and the individuals who donated their blood from which the ankyrin complex was purified. T.C. is supported by grants from the Italian Ministry of University and Research (Bando SIR 2014 grant nos. RBSI14C65Z and PRIN2017) and from the Universita' degli Studi di Padova (Progetto Giovani 2012 grant no. GRIC128SP0, Progetto di Ateneo 2016 no. CALI_SID16_01 and STARS consolidator grant no. 2019). Some of this work was performed at the SEMC, National Resource for Automated Molecular Microscopy and the National Center for In situ Tomographic Ultramicroscopy located at the New York Structural Biology Center, supported by grants from the Simons Foundation (no. SF349247) and NIH NIGMS (no. GM103310) and NIH (no. U24GM139171).

Author contributions

F.V., with the assistance of L.Y.Y., performed protein preparation for structural analysis. F.V. and T.C. prepared membranes from human erythrocytes. F.V. screened and optimized sample vitrification, and generated cryo-EM data. J.D.J. and A.J.N. carried out tomography data analysis. Single-particle cryo-EM data analysis and model building was conducted by O.B.C. The manuscript was written by O.B.C. and F.V. with input from T.C. Figures were prepared by K.K and F.V.

Competing interests

The authors declare no competing interests.

Additional information

Extended data are available for this paper at https://doi.org/10.1038/s41594-022-00792-w.

Supplementary information The online version contains supplementary material available at https://doi.org/10.1038/s41594-022-00792-w.

Correspondence and requests for materials should be addressed to Oliver Biggs Clarke.

Peer review information *Nature Structural & Molecular Biology* thanks Yifan Cheng, Werner Kühlbrandt and Ashley Toye for their contribution to the peer review of this work. Primary Handling editor: Florian Ullrich, in collaboration with the *Nature Structural & Molecular Biology* team. Peer reviewer reports are available.

Reprints and permissions information is available at www.nature.com/reprints.

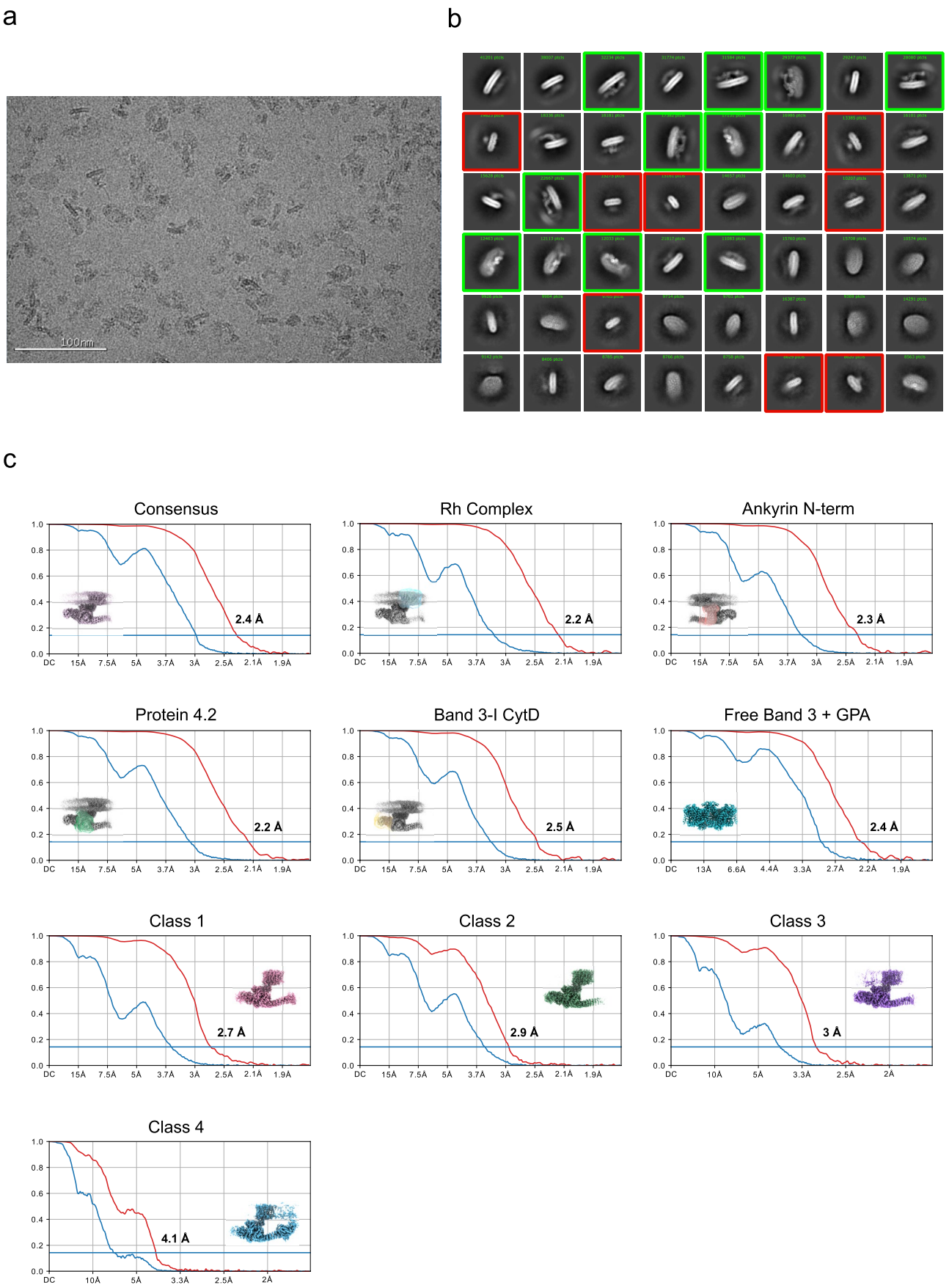

Extended Data Fig. 1 | Single particle cryo-EM structure determination. a, A representative micrograph out of 14.464 micrographs. **b**, 2D class averages of particles initially picked with Topaz (~1.8 M), ordered by population. 2D class averages of band 3–GPA (red box) and ankyrin-1 complexes (green box) are highlighted. **c**, Fourier shell correlation (FSC) curves. Maps shown as inset, with refinement mask in the case of local refinements.

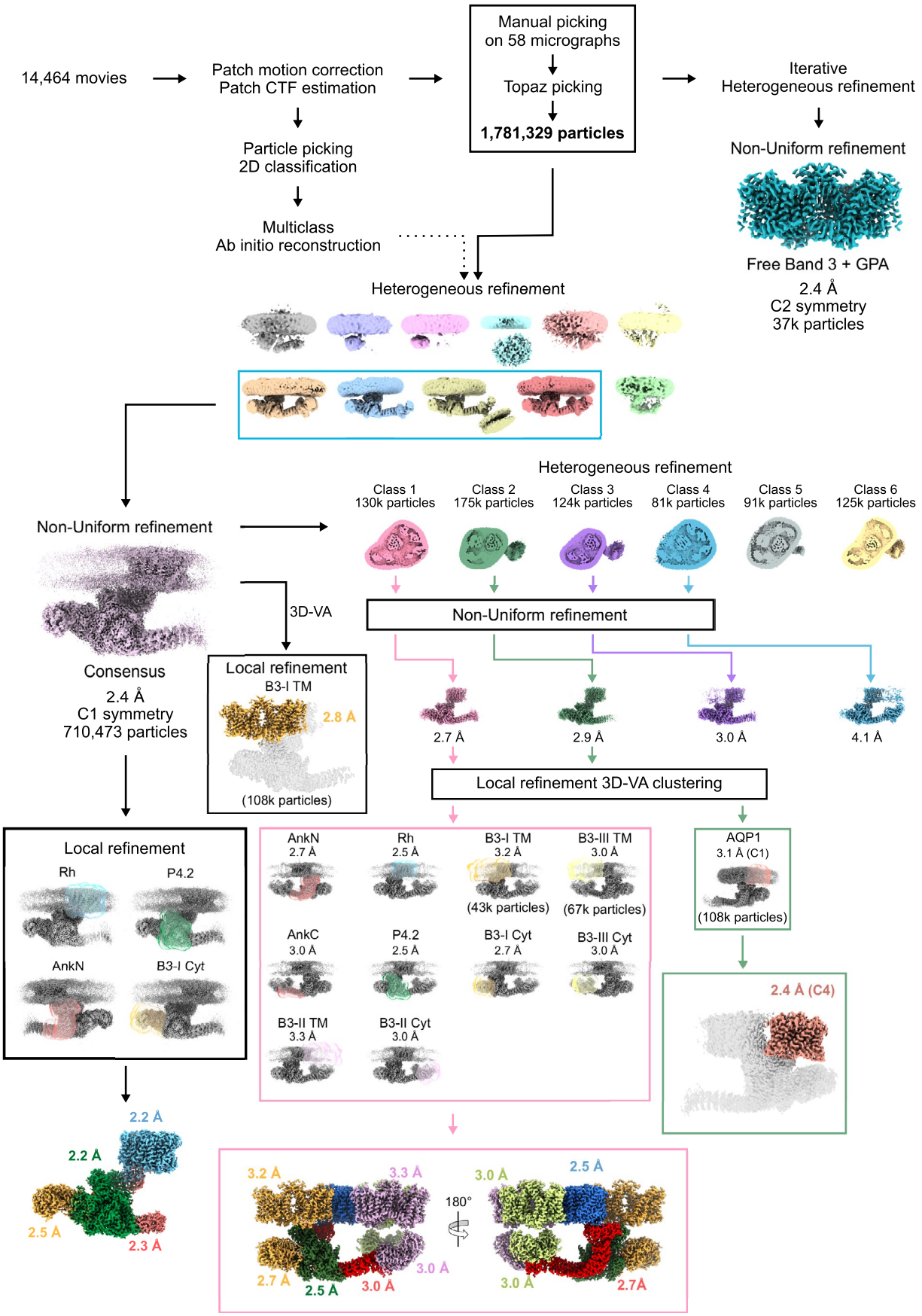

Extended Data Fig. 2 | Cryo-EM workflow and analysis of the ankyrin-1 complex. Flowchart outlining cryo-EM image acquisition and processing performed to obtain the structure of ankyrin-1 complex. All processing was performed using CryoSPARC v.3.3 (see Methods for details).

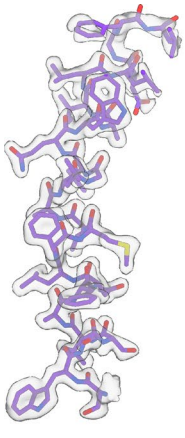

RhCE
(Ser73-Leu98)

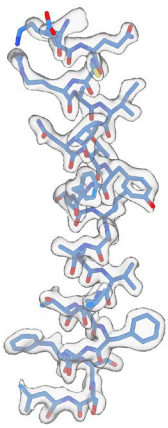

RhAG1
(Asp234-Leu260)

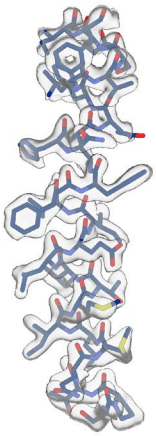

RhAG2
(Ser137-Phe163)

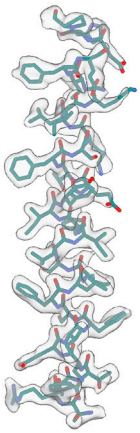

Free Band 3 (TM)
(Ser517-Pro548)

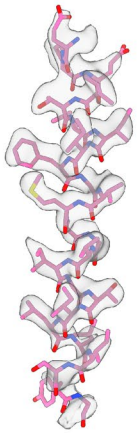

Glycophorin A
(Glu89-Gly113)

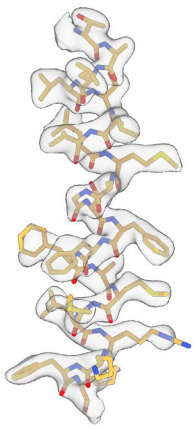

Band 3-I (TM)
(Thr570-Lys592)

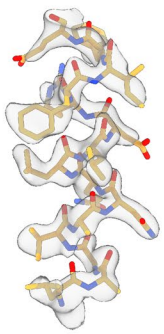

Band 3-I (Cyt)
(Leu128-Glu142)

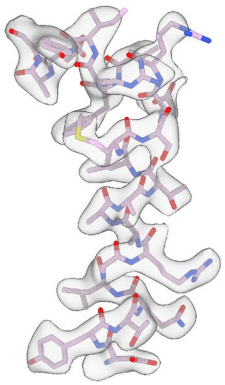

Band 3-II (Cyt)
(Asp277-Tyr299)

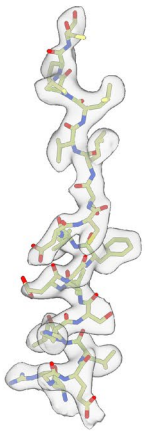

Band 3-III (Cyt)
(Arg304-Thr324)

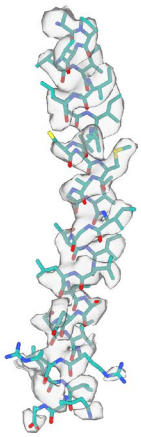

Glycophorin B
(Ala59-Ala91)

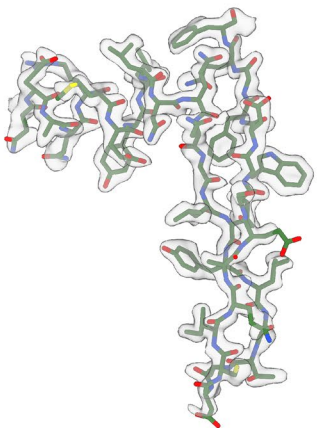

Protein 4.2
(Asn151-Phe184)

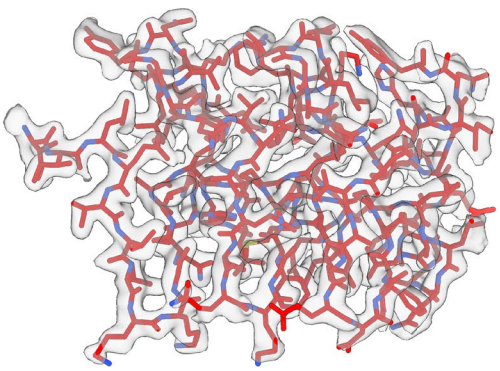

Ankyrin-1
(Ile69-Tyr166)

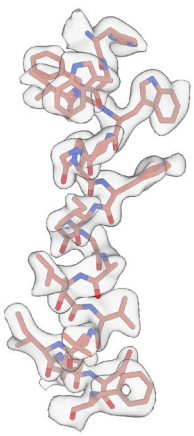

Aquaporin-1
(His209-Phe229)

Extended Data Fig. 3 | See next page for caption.

Extended Data Fig. 3 | Model/map fit. Cryo-EM densities (transparent gray surface) are shown with corresponding segments of the atomic model; sidechains are rendered in stick representation and colored as in Fig. 1. The densities for GPA and free band 3 are derived from the free band3 class. Density for band 3-I TM derives from local refinement of Class 3. For all the other images we used the density from local refinement of the consensus refinement.

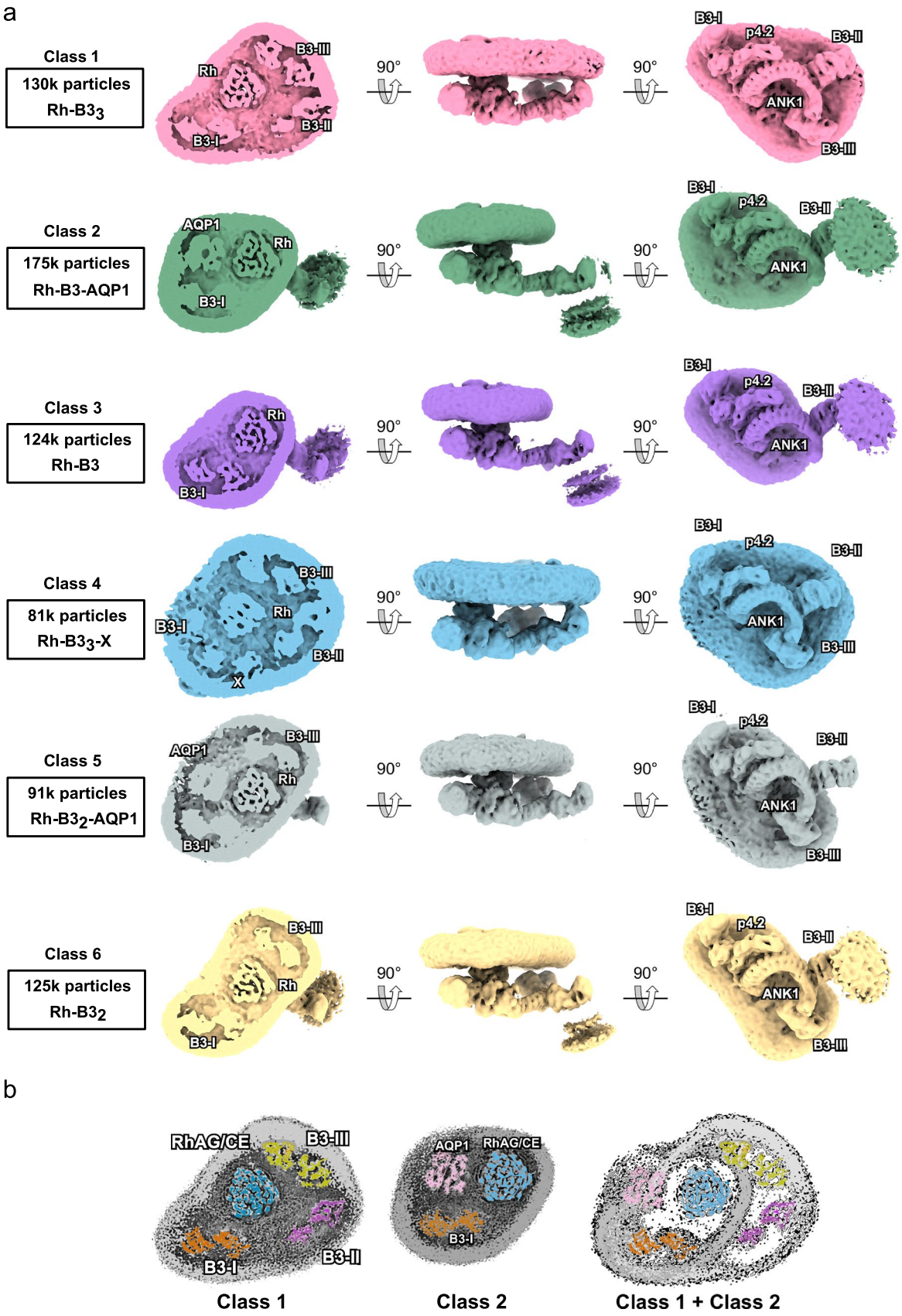

Extended Data Fig. 4 | See next page for caption.

Extended Data Fig. 4 | Ankyrin-1 complex classes. a, Different views of six main classes of the ankyrin-1 complex. Class 1 contains an $(RhAG)_2(RhCE)$ heterotrimer, ankyrin-1, protein 4.2, and three band 3 dimers (I, II, III). Class 2 exhibits a smaller micelle, retaining the core $(RhAG)_2(RhCE)(Ank1)(P4.2)$ architecture, but including only one band 3 dimer (B3-I), bound to protein 4.2, and aquaporin. Class 3 contains an $(RhAG)_2(RhCE)$ heterotrimer, and a single band 3 (B3-I). Class 4 has a bigger micelle and contains an $(RhAG)_2(RhCE)$ heterotrimer, ankyrin-1, protein 4.2, three band 3 dimers and an unidentified protein "X'. Class 5 contains an $(RhAG)_2(RhCE)$ heterotrimer, ankyrin-1, protein 4.2, aquaporin and Band 3-I and Band 3-III. Class 6 contains an $(RhAG)_2(RhCE)$ heterotrimer, ankyrin-1, protein 4.2, and Band 3-I and Band 3-III. In all the six classes the cytosolic domain of Band 3-II is present. The transmembrane domains of B3-II in classes 2, 3 and 6 appear to be associated with a separate micelle, likely due to either partial dissociation during extraction and/or re-association with free band 3 dimers post-extraction. **b**, Comparison of Class 1 & Class 2. Rh is colored in blue, Band 3-I in orange, Band 3-II in lilac, Band 3-III in yellow and aquaporin in pink. Superposition of Class 1 and Class 2 shows that presence of the additional two band 3 dimers does not exclude the presence of aquaporin.

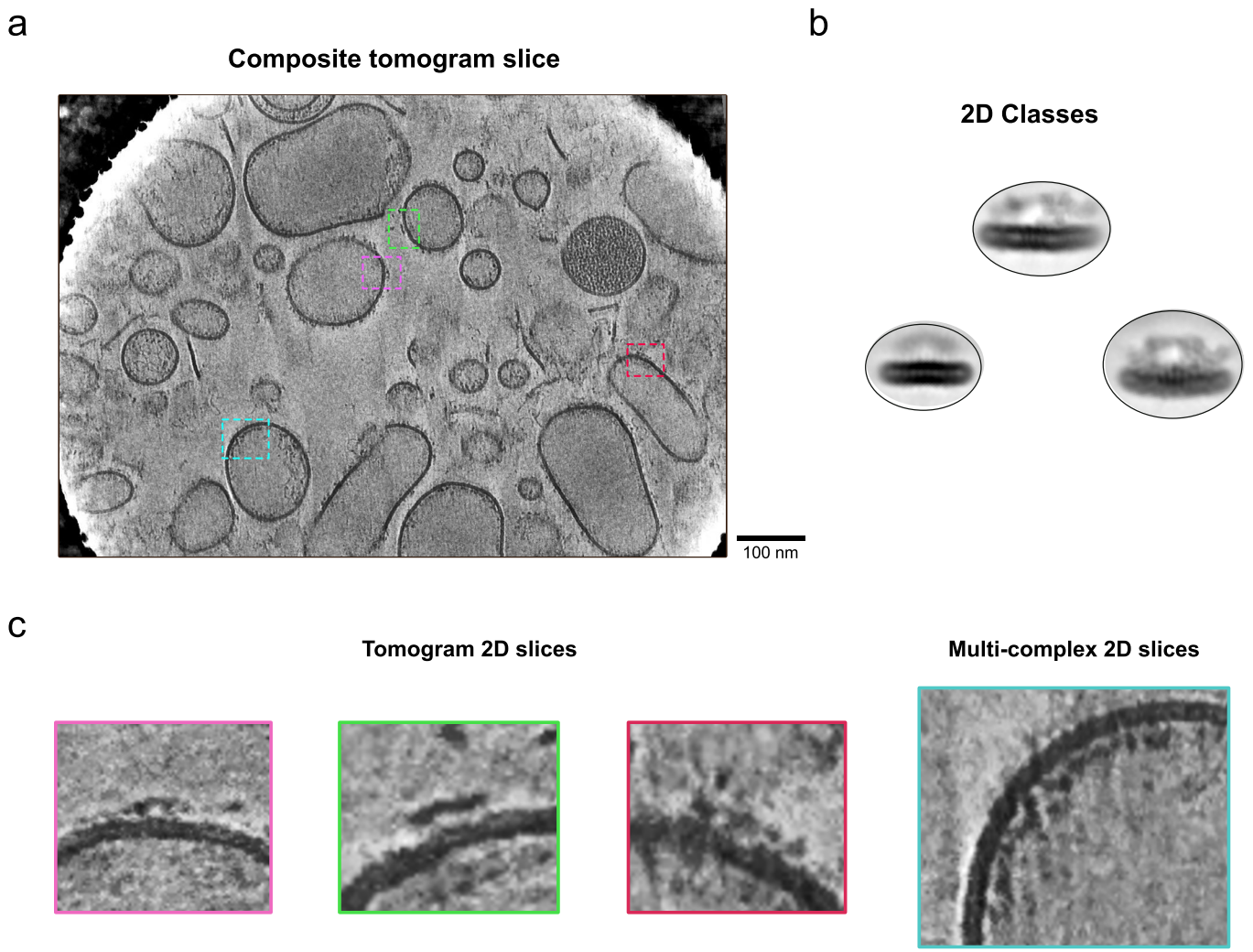

Extended Data Fig. 5 | Cryo-ET of native membrane vesicles. a, A composite slice from the tomogram shown in Supplementary Video 2 with several densities resembling ankyrin-1 complex side-views boxed out. **b**, SPA 2D class side-views for comparison with the tomogram slices. **c**, Magnified tomogram slices from the boxed-out regions in A. The multi-complex 2D slice on the right shows one of many visible strings of ankyrin-1 complex-like densities suggesting potential higher order assemblies. Tomogram slices are 8.3 Å thick. During the process of vesicle formation, vesicles can form in either the native or inverted configurations, with the cytosolic side of the membrane oriented in either direction.

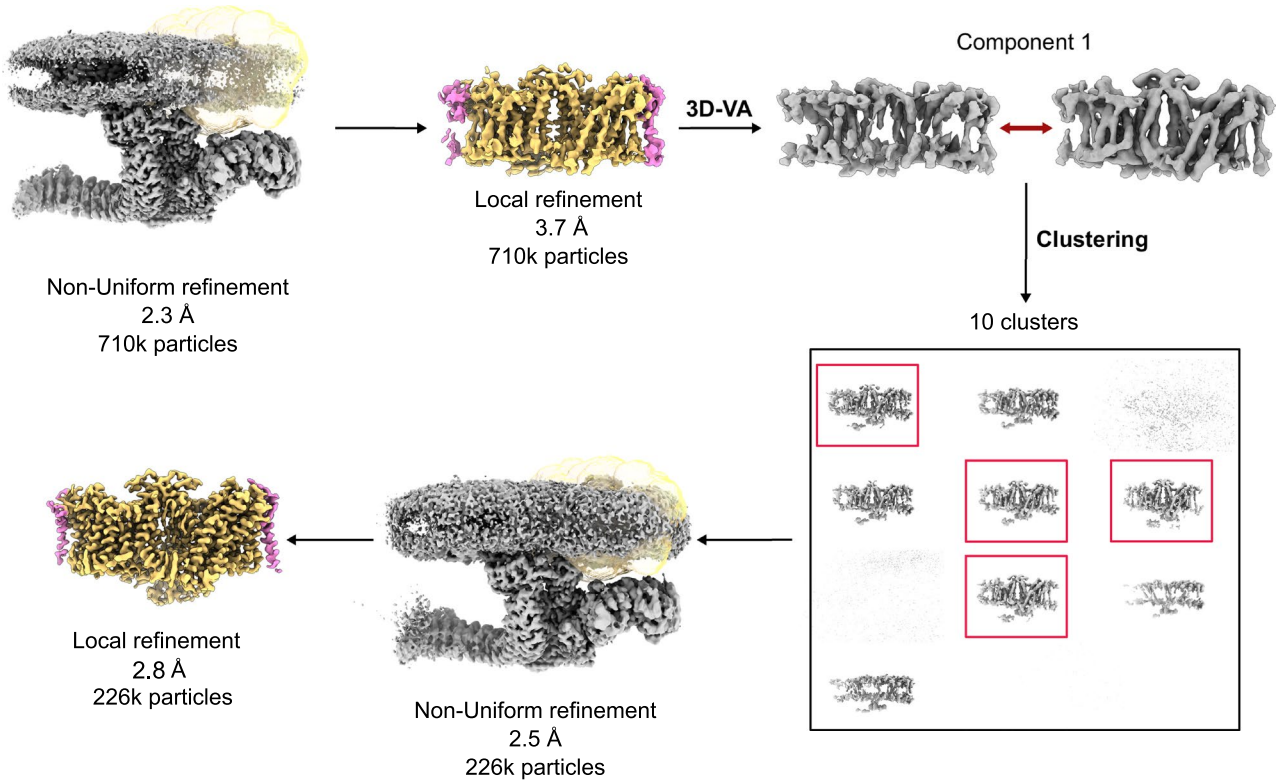

Extended Data Fig. 6 | Cryo-EM workflow for sub-classification of Band 3-I from the consensus refinement. Flowchart outlining cryo-EM processing performed to improve the structure of Band 3-I (orange) and the bound GPA proteins (magenta). All processing was performed using CryoSPARC v.3.3. A similar procedure was used to improve the density of AQP1 starting from Class 2.

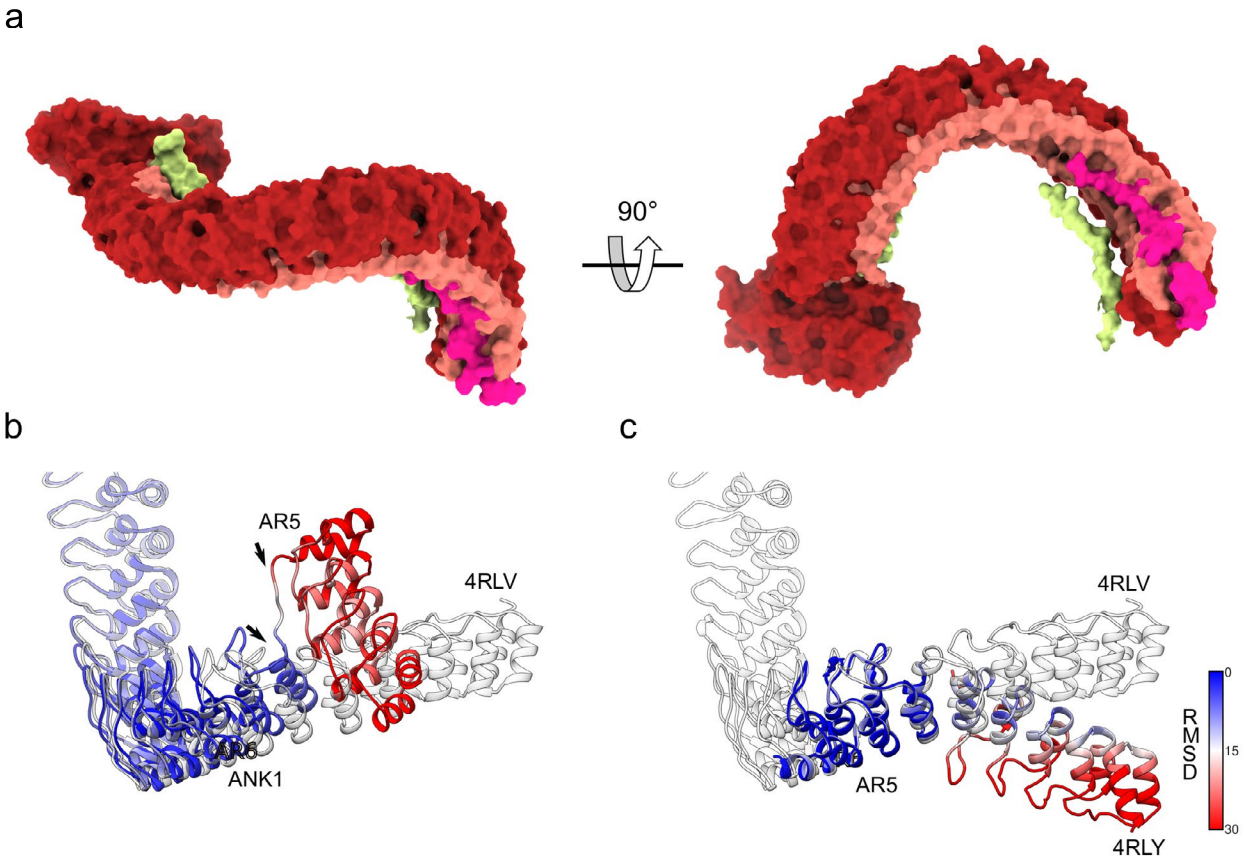

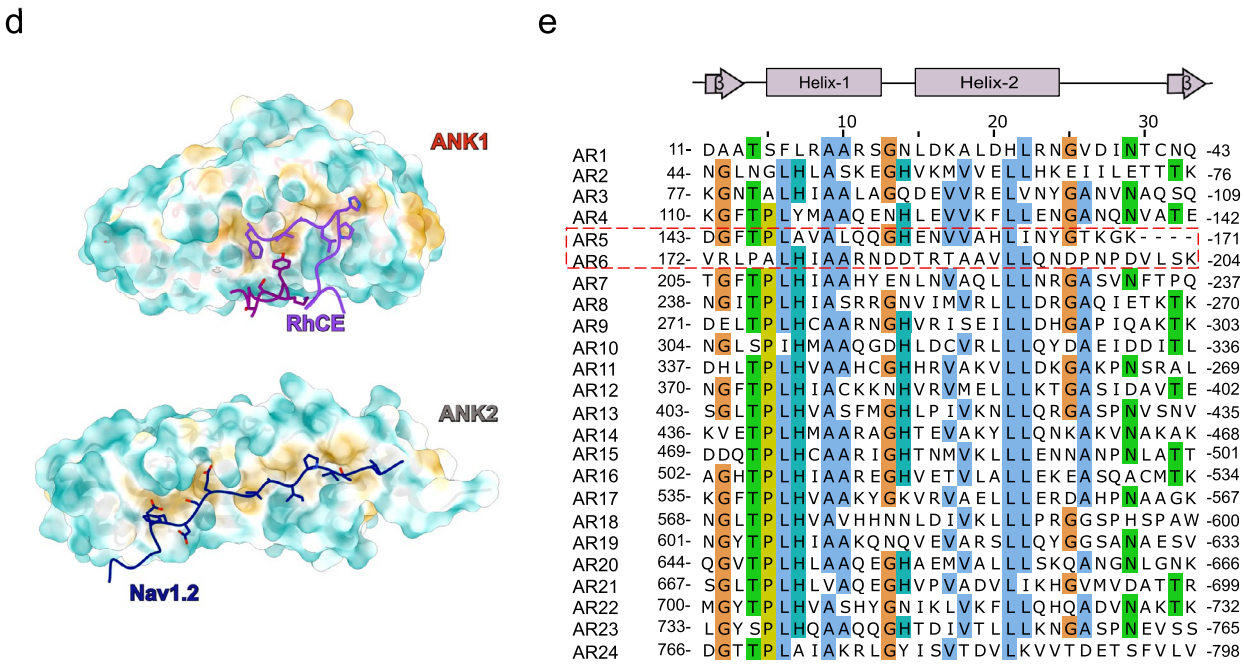

Extended Data Fig. 7 | See next page for caption.

Extended Data Fig. 7 | Conformation of membrane-associated ankyrin-1. a, Ankyrin structure shown as a molecular surface with the inner groove depicted in pink, the convex outer surface in red, in yellow the N-terminal peptide of Band 3-III and in magenta the C-terminal linker of ankyrin-1. **b**, Structural alignment between ankyrin-1 structure (colored by RMSD) and ankyrin-2 (in gray). The first 5 repeats of Ank1 are dramatically rearranged compared to their position in the Ank2 structure. Arrows indicate AR5 and 6. **c**, Structural alignment between ankyrin-2 (gray) and ankyrin-2 bound to Nav1.2 peptide (colored by RMSD), shows that flexibility at this interface also occurs in ankyrin-2. **d**, Hydrophobic surface calculated for the first 5 ankyrin repeats (AR1-5) of Ank1 (top) and Ank2 (bottom). RhCE N-terminal (magenta) and C-terminal fragments (purple) are displayed in stick representation. In the lower figure Ank2 is bound to Nav1.2 peptide (blue). **e**, Sequence alignment of all the 24 ankyrin repeats of Ank1 using MUSCLE[82] and visualized and colored using Jalview with the ClustalX color scheme. The sequences for AR5 and 6 are outlined in red. **f**, Sequence of AR5 and AR6 from Ank1, Ank2 and Ank3, aligned using MUSCLE [82] and visualized and colored using Jalview with the ClustalX colour scheme. The three sequences are well conserved in AR5 and 6. Arrows indicate the region that rearranges in Ank1. AR5 is shorter than the other repeats by 4 residues, and AR6 lacks both the "S/TP' motif at positions 4–5, and the consensus "GH' motif at positions 13–14 is replaced by two aspartates.

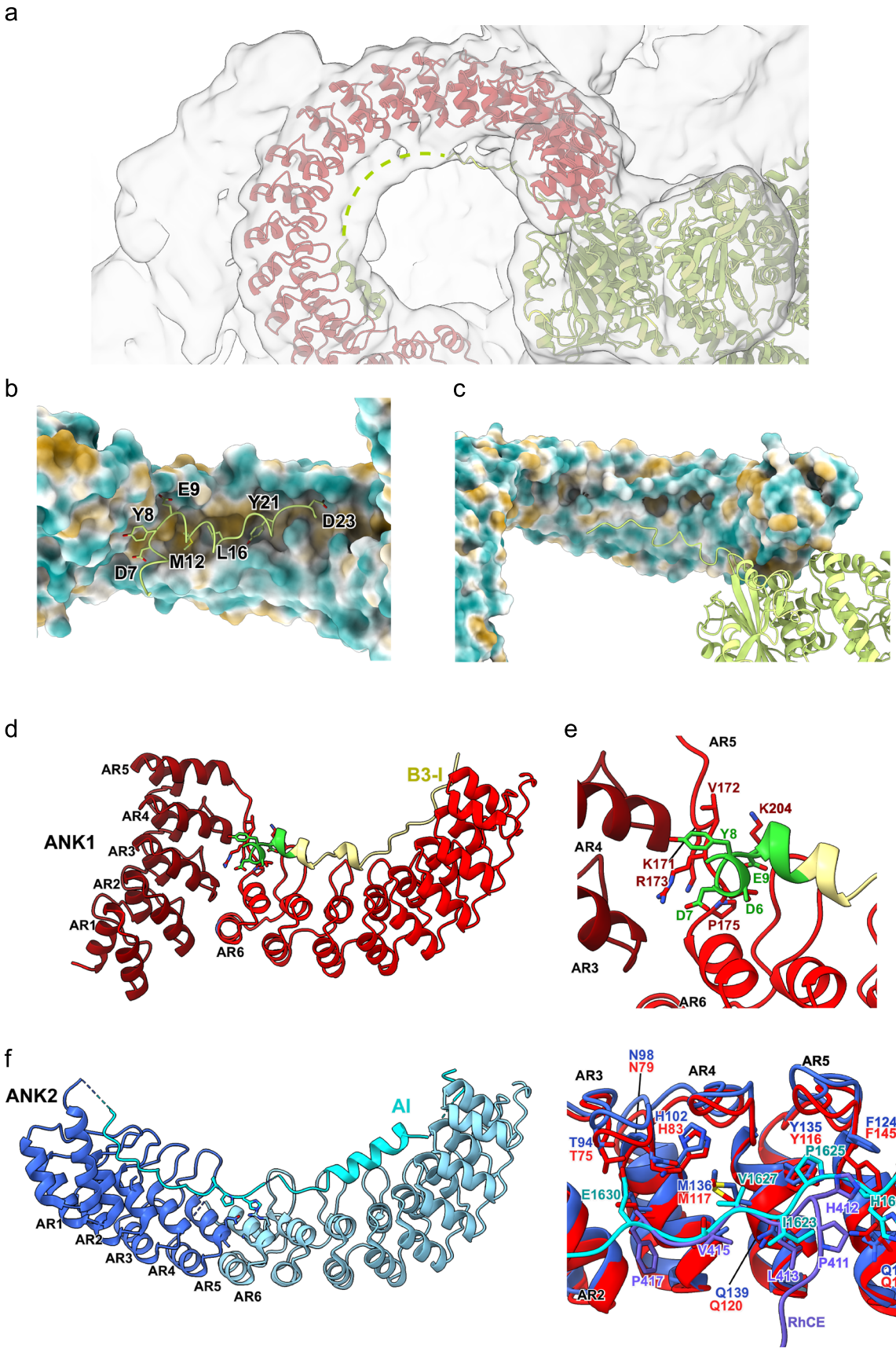

Extended Data Fig. 8 | See next page for caption.

Extended Data Fig. 8 | Ankyrin interaction with Band 3-III N-terminal peptide. a, Map at low density threshold allows tracing of the complete Band 3-III N-terminal peptide (dotted yellow line), that runs back along the inner ankyrin groove. **b-c**, Molecular surface of the ankyrin repeats, colored by hydrophobicity, bound to the N-terminal peptide of Band 3-III (yellow). Residues 2–24 of Band 3-III form an ordered interaction with AR6-10 and the AR5-6 linker. Key residues are displayed as sticks. Band 3-III is shown as yellow ribbons. **d**, Structural comparison between ankyrin-1 (top) and ankyrin-2 structures (PDB: 4Y4D) (bottom). Structure of ankyrin-1 (dark red AR1-5 and red AR6-12) is associated with N-terminal peptide of Band 3-I (yellow) and ankyrin-2 (dark blue AR1-6 and light blue AR6-12) is associated with the autoinhibitory domain (AI) of ankyrin-1. **e**, Close up of the AR5-6 of ankyrin-1 in panel S8d. The Band 3-I part colored in green corresponds to the first 11 N-terminal amino acids. **f**, Structural alignment between the first five ankyrin repeats (AR1-5) of ankyrin-1 (dark red) bound to RhCE peptide and ankyrin-2 (dark blue) bound to the autoinhibitory peptide of ankyrin-1. The key conserved residues that mediate the interactions between ANK1 and B3-III and ANK2 and the autoinhibitory region are shown as sticks.

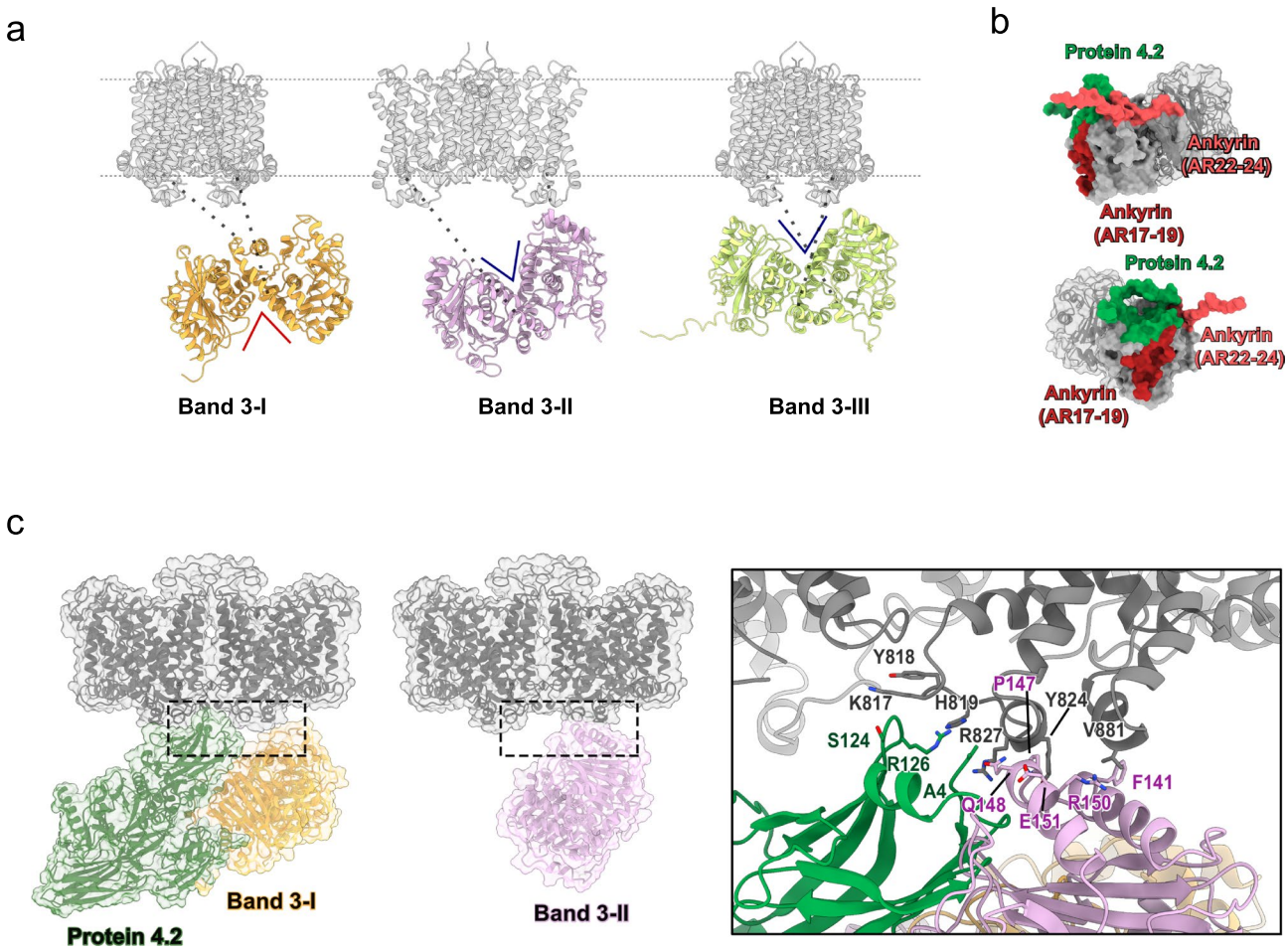

Extended Data Fig. 9 | Flexibility of band 3 cytosolic domain. a, Models of the three Band 3 dimers (I, II, III). The three cytosolic domains of Band 3 proteins in the complex have different orientations. The Band 3-I cytoplasmic domain is inverted with respect to those of Band 3-II and Band 3-III. The TM part of Band 3 is colored gray. **b**, Two different views of band 3 cytosolic domain represented as molecular surface. Interacting surfaces of band 3 are distinct and non-overlapping. Regions of the band 3 cytosolic domain that interact with proteins in the complex are shown in different colors: green for the region that interact with protein 4.2, red for ankyrin repeats 22–24 and purple for ankyrin repeats 17–19. **c**, Comparison between Band 3-I (yellow) associated with protein 4.2 (green) and Band 3-II (lilac). The model is displayed as ribbon and the surface is shown in transparency. In the right panel a close view of the interactions between Band 3-II cytosolic domain (lilac) and protein 4.2 (green); the two share the same interaction site with the TM part. Key residues for the interaction are displayed as sticks.

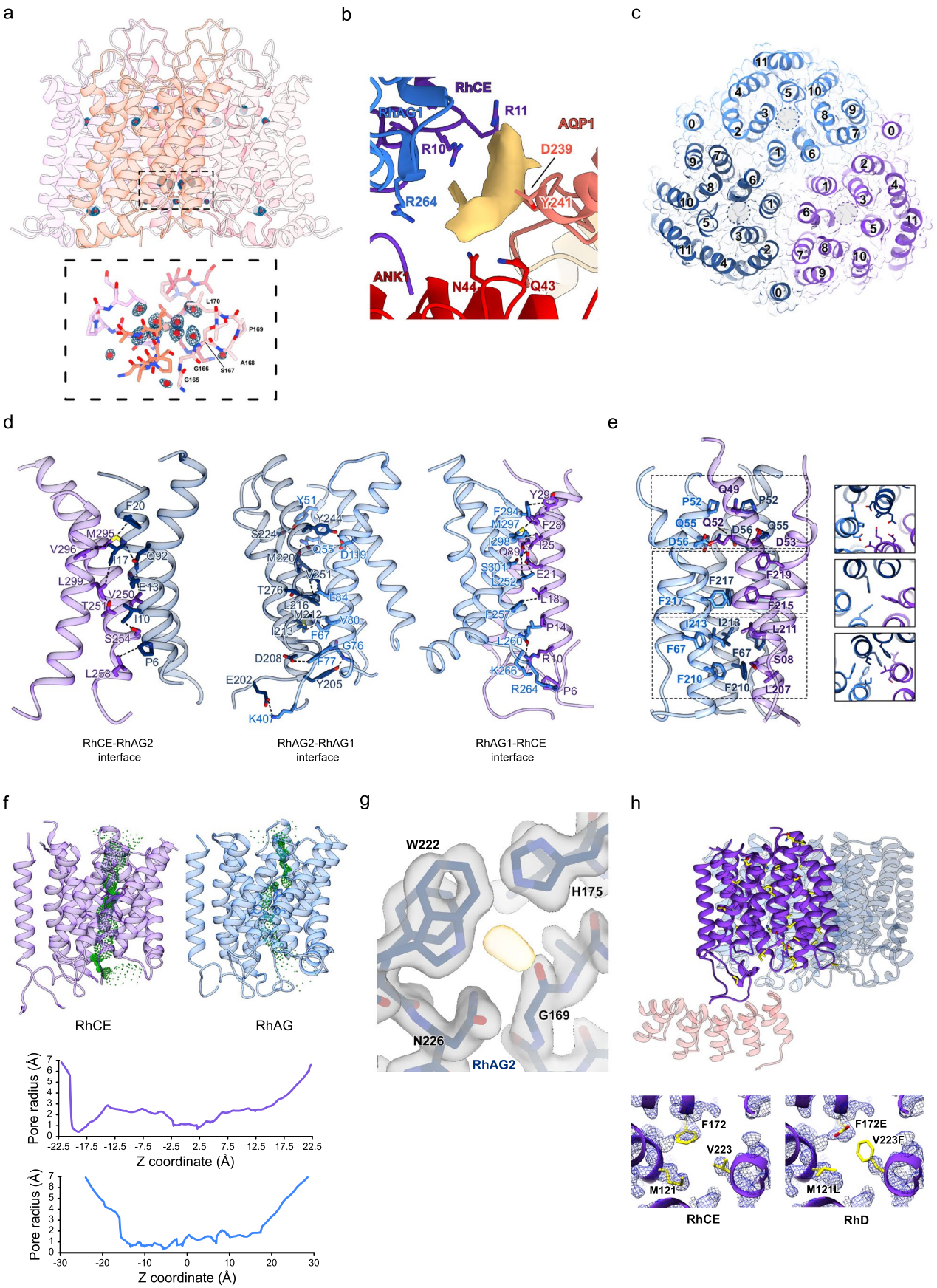

Extended Data Fig. 10 | See next page for caption.

Extended Data Fig. 10 | $(RhAG)_2(RhCE)$ trimer interactions. a, Model of AQP1 with waters (red dots fit inside the map). In the bottom inset a close view of the waters in the central cavity. **b**, Unmodeled density at the interface of aquaporin-1 (salmon) with RhCE (purple) and RhAG (light blue). Potential interacting sidechains are depicted in stick representation. **c**, The structure of $(RhAG)_2(RhCE)$ trimer as viewed from the cytoplasm, RhCE is colored in purple, RhAG1 in light blue and to RhAG2 in dark blue. The cryo-EM density map of the $(RhAG)_2(RhCE)$ trimer is shown in transparency. The 12 TM helixes are numbered (0–11) for each Rh molecule. Gray circles shown the pore position in each subunit. **d**, Interfaces between the three different subunits, with key residues represented as sticks. **e**, Interface between the three Rh protomers. The key residues that mediate the interactions in the interfaces are shown as sticks. Three different parts of the trimerization interface are show in the right figure viewed from the top. **f**, Analysis of the pores of RhCE and RhAG. Figure of the pore in green generated by HOLE. 2D graph of pore radius for RhCE (top graph) and RhAG (bottom graph). **h**, Close up of RhAG2, the map shows an undefine density. The key residues that interact with the undefined density are shown as sticks. **g**, Structure of $(RhAG)_2(RhCE)$ complex and the first five repeats of ankyrin. The amino acids depicted in yellow sticks highlight the sites of variation between RhCE and RhD. Three sites of variation between RhD and RhCE are shown in the right panels, with the density map overlayed. The density map is consistent with the presence of RhCE, not RhD.

nature portfolio

Corresponding author(s): Oliver B. Clarke

Last updated by author(s): May 14, 2022

Reporting Summary

Nature Portfolio wishes to improve the reproducibility of the work that we publish. This form provides structure for consistency and transparency in reporting. For further information on Nature Portfolio policies, see our Editorial Policies and the Editorial Policy Checklist.

Statistics

For all statistical analyses, confirm that the following items are present in the figure legend, table legend, main text, or Methods section.

n/a	Confirmed
☐	☒ The exact sample size (*n*) for each experimental group/condition, given as a discrete number and unit of measurement
☒	☐ A statement on whether measurements were taken from distinct samples or whether the same sample was measured repeatedly
☒	☐ The statistical test(s) used AND whether they are one- or two-sided *Only common tests should be described solely by name; describe more complex techniques in the Methods section.*
☒	☐ A description of all covariates tested
☒	☐ A description of any assumptions or corrections, such as tests of normality and adjustment for multiple comparisons
☒	☐ A full description of the statistical parameters including central tendency (e.g. means) or other basic estimates (e.g. regression coefficient) AND variation (e.g. standard deviation) or associated estimates of uncertainty (e.g. confidence intervals)
☒	☐ For null hypothesis testing, the test statistic (e.g. *F*, *t*, *r*) with confidence intervals, effect sizes, degrees of freedom and *P* value noted *Give P values as exact values whenever suitable.*
☒	☐ For Bayesian analysis, information on the choice of priors and Markov chain Monte Carlo settings
☒	☐ For hierarchical and complex designs, identification of the appropriate level for tests and full reporting of outcomes
☒	☐ Estimates of effect sizes (e.g. Cohen's *d*, Pearson's *r*), indicating how they were calculated

Our web collection on statistics for biologists contains articles on many of the points above.

Software and code

Policy information about availability of computer code

Data collection	Leginon 3.5
Data analysis	For Cryo-EM data processing the following software were used: Appion 3.4, cryoSPARC 3.2-3.3, Topaz 0.2.4 For model building , the following software were used: Coot 0.9.6, Phenix 1.19, Chimera 1.15 , ChimeraX 1.3, HOLE v2.2.005 For sequence alignment the following software were used: Muscle 3.8, Jalview 2.11.1.4 For mass photometry: AcquireMP v2.3, DiscoverMP v2.3 For cryoET data collection and processing: MotionCor2, Appion-Protomo v1.2.2, Tomo3D v2.0, Warp v1.0.9, IMOD v4.11, AreTomo v1.0.12, crYOLO v1.8, Relion v4.0

For manuscripts utilizing custom algorithms or software that are central to the research but not yet described in published literature, software must be made available to editors and reviewers. We strongly encourage code deposition in a community repository (e.g. GitHub). See the Nature Portfolio guidelines for submitting code & software for further information.

Data

Policy information about availability of data

All manuscripts must include a data availability statement. This statement should provide the following information, where applicable:

- Accession codes, unique identifiers, or web links for publicly available datasets
- A description of any restrictions on data availability
- For clinical datasets or third party data, please ensure that the statement adheres to our policy

All raw movie files, aligned micrographs, and particle coordinates are deposited in the EMPIAR (EMPIAR-11043). All relevant protein structure models will be

deposited in the PDB (PDB IDs:7UZ3, 7UZE, 7UZQ, 7UZS, 7UZU, 7UZV,7V07, 7V0K, 7V0M, 7V0Q, 7V0S, 7V0T, 7V0U, 7V0X, 7V0Y, 7V19, 8CRQ, 8CRR, 8CRT, 8CS9, 8CSV, 8CSW, 8CSX, 8CSY, 8CT2, 8CT3, 8CSL, 8CTE). CryoEM maps, halfmaps, and masks will be deposited in the EMDB (EMDB IDs:EMD-26874, EMD- 26886, EMD-26916, EMD-26917, EMD-26918, EMD-26919, EMD-26940, EMD-26943, EMD-26944, EMD-26948, EMD-26949, EMD-26950, EMD-26951, EMD-26952, EMD-26953, EMD-26954, EMD-26955, EMD-26956, EMD-26958, EMD-26960, EMD-26972, EMD-26973, EMD-26974, EMD-26975, EMD-26978, EMD-26979, EMD-26982, EMD-26965, EMD-26988).

Field-specific reporting

Please select the one below that is the best fit for your research. If you are not sure, read the appropriate sections before making your selection.

☒ Life sciences ☐ Behavioural & social sciences ☐ Ecological, evolutionary & environmental sciences

For a reference copy of the document with all sections, see nature.com/documents/nr-reporting-summary-flat.pdf

Life sciences study design

All studies must disclose on these points even when the disclosure is negative.

Sample size	14.464 micrographs
Data exclusions	Only bad micrographs were excluded for analysis.
Replication	Multiple replicates of cryoEM grids were made with varying blot parameters.
Randomization	Randomization is not relevant to this structural study.
Blinding	Blinding is not relevant to this structural study.

Reporting for specific materials, systems and methods

We require information from authors about some types of materials, experimental systems and methods used in many studies. Here, indicate whether each material, system or method listed is relevant to your study. If you are not sure if a list item applies to your research, read the appropriate section before selecting a response.

Materials & experimental systems

n/a	Involved in the study
☒	☐ Antibodies
☒	☐ Eukaryotic cell lines
☒	☐ Palaeontology and archaeology
☒	☐ Animals and other organisms
☒	☐ Human research participants
☒	☐ Clinical data
☒	☐ Dual use research of concern

Methods

n/a	Involved in the study
☒	☐ ChIP-seq
☒	☐ Flow cytometry
☒	☐ MRI-based neuroimaging